remote sensing

MDPI

Article

Forecasting Flood Inundation in U.S. Flood-Prone Regions Through a Data-Driven Approach (FIER): Using VIIRS Water Fractions and the National Water Model

Amirhossein Rostami [1], Chi-Hung Chang [1], Hyongki Lee [1,*], Hung-Hsien Wan [1], Tien Le Thuy Du [1], Kel N. Markert [2], Gustavious P. Williams [2], E. James Nelson [2], Sanmei Li [3], William Straka III [4], Sean Helfrich [5] and Angelica L. Gutierrez [6]

[1] Department of Civil & Environmental Engineering, University of Houston, 5000 Gulf Fwy, Bldg. 4, Rm#216, Houston, TX 77204, USA; arostami@cougarnet.uh.edu (A.R.); cchang37@cougarnet.uh.edu (C.-H.C.); hwan5@cougarnet.uh.edu (H.-H.W.); ldu10@cougarnet.uh.edu (T.L.T.D.)
[2] Department of Civil and Construction Engineering, Brigham Young University, Engineering Building 430, Provo, UT 84602, USA; km0033@student.byu.edu (K.N.M.); gus.williams@byu.edu (G.P.W.); jimn@byu.edu (E.J.N.)
[3] Department of Geography and Geoinformation Science, George Mason University, 4400 University Dr., Fairfax, VA 22030, USA; slia@gmu.edu
[4] Space Science and Engineering Center, University of Wisconsin—Madison, 1225 W. Dayton St., Madison, WI 53706, USA; wstraka@ssec.wisc.edu
[5] National Environmental Satellite Data and Information Service, National Oceanic and Atmospheric Administration, 1335 East-West Highway, SSMC1 8th Floor Suite 8300, Silver Spring, MD 20910, USA; sean.helfrich@noaa.gov
[6] Office of Water Prediction, National Weather Service, National Oceanic and Atmospheric Administration, 1325 East-West Highway, Silver Spring, MD 20910, USA; angelica.gutierrez@noaa.gov
* Correspondence: hlee45@central.uh.edu

Citation: Rostami, A.; Chang, C.-H.; Lee, H.; Wan, H.-H.; Du, T.L.T.; Markert, K.N.; Williams, G.P.; Nelson, E.J.; Li, S.; Straka III, W.; et al. Forecasting Flood Inundation in U.S. Flood-Prone Regions Through a Data-Driven Approach (FIER): Using VIIRS Water Fractions and the National Water Model. *Remote Sens.* **2024**, *16*, 4357. https://doi.org/10.3390/rs16234357

Academic Editor: Valeria Satriano

Received: 17 September 2024
Revised: 19 November 2024
Accepted: 20 November 2024
Published: 22 November 2024

Abstract: Floods, one of the costliest, and most frequent hazards, are expected to worsen in the U.S. due to climate change. The real-time forecasting of flood inundations is extremely important for proactive decision-making to reduce damage. However, traditional forecasting methods face challenges in terms of implementation and scalability due to computational burdens and data availability issues. Current forecasting services in the U.S. largely rely on hydrodynamic modeling, limited to river reaches near in situ gauges and requiring extensive data for model setup and calibration. Here, we have successfully adapted the Forecasting Inundation Extents using REOF (FIER) analysis framework to produce forecasted water fraction maps in two U.S. flood-prone regions, specifically the Red River of the North Basin and the Upper Mississippi Alluvial Plain, utilizing Visible Infrared Imaging Radiometer Suite (VIIRS) optical imagery and the National Water Model. Comparing against historical VIIRS imagery for the same dates, FIER 1- to 8-day medium-range pseudo-forecasts show that about 70–80% of pixels exhibit absolute errors of less than 30%. Although originally developed utilizing Synthetic Aperture Radar (SAR) images, this study demonstrated FIER's versatility and effectiveness in flood forecasting by demonstrating its successful adaptation with optical VIIRS imagery which provides daily water fraction product, offering more historical observations to be used as inputs for FIER during peak flood times, particularly in regions where flooding commonly happens in a short period rather than following a broad seasonal pattern.

Keywords: VIIRS water fractions; national water model; flood forecasting; EOF analysis

1. Introduction

Floods are among the most devastating hazards in the world, causing extensive damage to human lives, property, and agriculture. From 1980 to 2024, the U.S. experienced 42 riverine and urban flooding events, resulting in a total cost of $200.7 billion and 738 deaths [1]. Future flood exposure and damage in the U.S. are expected to worsen due to

anthropogenic climate change, population growth, and urban development [2–4]. Precipitation extremes are expected to increase nonlinearly under a warming climate, intensifying flood impacts [5]. Therefore, reliable real-time forecasts are essential for mitigating flood damage, enabling timely response, and enhancing preparedness [6,7].

Hydrodynamic modeling is a widely used method for simulating flood inundation behavior [8]. However, it demands significant data and computational resources, limiting its practicality for real-time forecasting, especially when this has to be performed consistently over large areas for rapid response [9–12]. The high data requirements include boundary and initial condition data, topography and bathymetry data, details of any existing hydraulic structures, and friction coefficients for the energy loss mechanisms, all of which impact modeling accuracy [13]. Furthermore, acquiring these data, often from costly sources like in situ gauges, field surveys, and Light Detection and Ranging (LiDAR) data, hinders scalability. Indeed, despite the operational flood inundation mapping offered by the United States Geological Survey (USGS) Flood Inundation Mapper (FIM) [14], and the National Weather Service (NWS) Advanced Hydrologic Prediction Service (AHPS) flood inundation mapping system [15] at over 150 locations in the U.S., with a pre-simulating library of inundation maps from hydrodynamic modeling, their coverages are limited to areas near gauges. Efforts have been made to address the computational burden of hydrodynamic models by developing surrogate modeling approaches suitable for real-time forecasts [16]. For instance, Ivanov et al. [17] proposed a real-time urban flood forecasting framework that decomposes the response of a high-fidelity model into a set of quantities of interest (QoIs), such as water depth, which are estimated using pre-trained surrogate models. This approach reduces computational costs and accelerates the flood simulation process. However, access to high-performance computing facilities is still necessary to run numerous simulations of the high-fidelity models and train the surrogates, which remains a significant challenge.

The Height Above Nearest Drainage (HAND) approach is another well-recognized approach capable of generating flood inundation maps, using terrain data to determine relative heights with respect to the nearest stream cell [18]. Areas become inundated if their relative heights fall below the water stages of the nearest stream cells [19,20]. In real-time forecasting, hydrological models can provide streamflow forecasts at the stream cell, which can then be converted to water stages using synthetic rating curves [21]. The HAND approach is computationally efficient and cost-effective for estimating flood inundations and thus is used by the Office of Water Prediction (OWP) at the National Water Center (NWC) of NOAA, along with the National Water Model (NWM) [22]. However, the HAND approach does not conserve volume, assuming an infinite water supply to flood all areas below stream stages [9]. Its performance is highly sensitive to the quality of the base topography data, especially in low-relief areas, where small errors in the water stages can result in significant errors in the simulated flood maps. A recent study in the U.S. found potential overestimations in flat terrain, even with the 10 m spatial resolution National Elevation Dataset (NED 10 m) Digital Elevation Model (DEM) generated from the LiDAR data and aerial photography [23]. Moreover, HAND-simulated flood inundations can be sensitive to the friction coefficients in the synthetic rating curves, with tributaries requiring higher coefficients to avoid flood underestimations [23].

In hydrology, the use of remotely sensed imagery for flood monitoring and hydrodynamic model calibration has grown steadily since the 1970s, with the launch of Landsat-1 [24]. Numerous remote sensing satellites, equipped with either optical (multispectral or hyperspectral) or Synthetic Aperture Radar (SAR) sensors, have provided consistent and repetitive observations of surface water with stable quality. Chang et al. [25] leveraged the capabilities of remote sensing imagery to introduce an innovative data-driven framework for flood inundation forecasting, later named Forecasting Inundation Extents using Rotated Empirical Orthogonal Function (REOF) analysis (FIER) [26]. FIER effectively predicts flood signals by establishing relationships between historical satellite-observed flood inundations and hydrological data (e.g., water level and streamflow), bypassing the

aforementioned data requirements of hydrodynamic modeling and the HAND approaches, thus ensuring scalability. In addition, it demonstrates computational efficiency, simulating flood inundations within seconds, adding substantial practical value for real-time inundation forecasting.

Initially piloted in the Tonle Sap Lake floodplains in Cambodia, FIER utilized Sentinel-1 SAR intensity imagery, satellite altimetric water levels, and the El Niño index [25]. Subsequently, an operational flood inundation forecasting web application, named FIER-Mekong (https://fier-mekong.streamlit.app/ (accessed on 17 September 2024)), was developed for the entire floodplains of the Lower Mekong River Basin. This region poses challenges for hydrodynamic modeling due to its highly complex hydraulic conditions. Furthermore, the efficiency of HAND approach decreases in this region with flat terrain since it relies on DEM to calculate the distance from each cell to the nearest drainage, making it highly sensitive to DEM inaccuracies. Specifically, in areas of flat terrain where microtopography plays a significant role in water movement, the absence of clear drainage pathways can lead to misrepresentations of flood inundation extents. Therefore, small errors in DEM can lead to substantial inaccuracies in HAND's predicted flood extents. Hence, FIER-Mekong also leveraged the Variable Infiltration Capacity (VIC) hydrological model, which is fed by inputs including land cover, soil type, and metrological forcing (e.g., precipitation and wind speed) to simulate discharge. The discharge is then converted to water level using a water level-to-discharge rating curve. This enabled FIER-Mekong to generate daily flood inundation forecasts within a couple of hours (including the time required for VIC simulation) on a 2.10 GHz 24-Core Intel Xeon Platinum processor, with lead times of up to 18 days. In addition, the application has been extended to forecast flood inundation depths and the resulting damage to rice crops [26].

This study represents the first implementation of FIER in the United States, using optical satellite images. The chosen test regions, the Red River of the North Basin (RRNB), and the Upper Mississippi Alluvial Plain (UMAP), have recently experienced historic flood events and continue to face significant flood risks, as highlighted by local media [27,28]. Primarily comprising croplands, these areas are highly vulnerable to crop production losses. Nonetheless, the existing operational USGS FIM and NOAA AHPS systems do not currently simulate flood inundations in these regions.

As a data-driven framework dependent on observed historical flood events captured in satellite imagery for forecasting, FIER requires satellite imagery with a sufficient amount of flood inundation observations. Unlike the floodplains of the Lower Mekong River Basin, where flooding is governed by a seasonal monsoon lasting several months, flooding in the RRNB and UMAP is primarily caused by spring snowmelt and rainfall, with a shorter duration from late Spring to early Summer. More specifically, flooding in most of the flood-prone regions globally does not follow the ideal sinusoidal patterns; rather, rainfall is often concentrated in a short period, resulting in sudden peaks in streamflow lasting only one or two months, while the rest of the year is almost dry. Since FIER is a data-driven flood forecasting method which needs to be trained with satellite remote sensing images acquired during the peak flow period, the 12-day repeat period of Sentinel-1 SAR imagery, used in previous FIER frameworks, misses numerous flood inundation events (see Figure 1). The blue lines in the top panel of Figure 1 show the USGS in situ streamflow data from 2017 to the end of 2020 at gauges located in (a) Drayton, North Dakota, along the Red River of the North mainstem, and (b) New Madrid, Missouri, along the Mississippi River mainstem. High streamflow mostly occurs from late spring to early summer, with a short peak-streamflow period, particularly in the RRNB, leading to limited Sentinel-1 image acquisitions during peak flood events, as indicated by the green triangles. The bottom panel of Figure 1 highlights the limited number of Sentinel-1 image acquisitions, with only about 10 images during periods of streamflow higher than the 95th percentile.

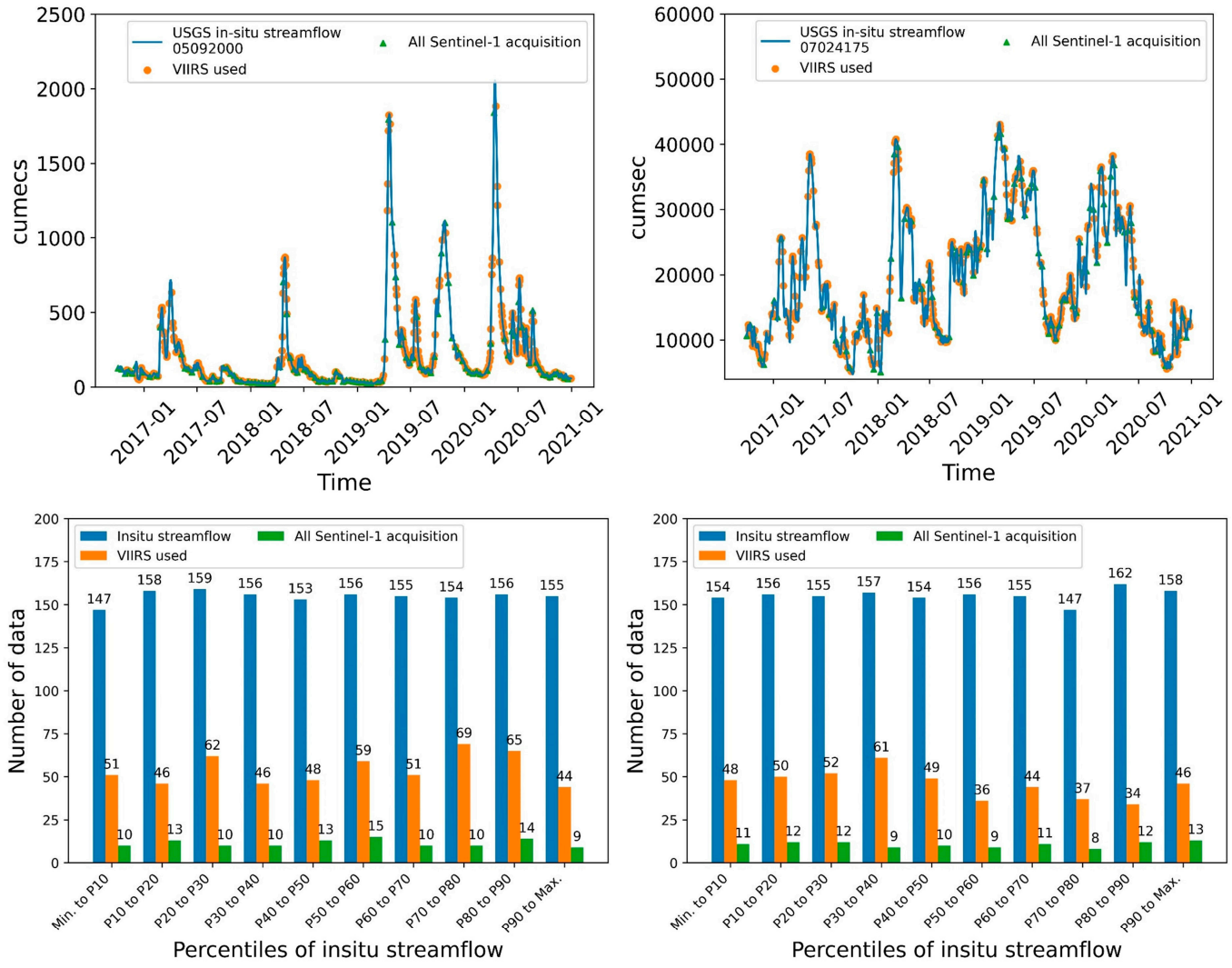

(a) (b)

Figure 1. (**top**) The USGS in situ streamflow data (blue line, cumecs: m^3/second) from 2017 to 2020 at gauges located in (**a**) Drayton, North Dakota, along the Red River of the North mainstem, and (**b**) New Madrid, Missouri, along the Mississippi River mainstem. The green triangles mark all the epochs when Sentinel-1 images were acquired, while the orange dots mark the epochs of the VIIRS images used in this study. (**bottom**) The corresponding amount of data with less than 5% cloud coverage within each of the 10% USGS in situ streamflow percentile groups.

Hence, we explored, for the first time, the feasibility of utilizing images captured by the Visible Infrared Imaging Radiometer Suite (VIIRS) optical sensors onboard the Suomi National Polar-orbiting Partnership (Suomi-NPP, launched in 2011), NOAA-20 (launched in 2017), and NOAA-21 (launched in 2022) weather satellites for constructing the FIER framework. The VIIRS imagery is known to be superior to the MODerate resolution Imaging Spectroradiometer (MODIS) imagery in flood detection [29,30] (see Section 3.1 for details).

To overcome the abovementioned limitations of the previous FIER framework, which employed Sentinel-1 data, this study aims to propose a more versatile flood forecasting approach by the following contributions:

- The VIIRS daily water fraction product is utilized to increase the amount of input data concurrent with peak streamflow periods, enabling FIER to be trained with more flood-relevant data compared to Sentinel-1.
- The NWM medium- and long-range streamflow forecast data are ingested into FIER to demonstrate the potential of being an operational flood forecasting tool.

Accordingly, we extracted flood-relevant spatiotemporal patterns (see Section 4.1) from historical daily composite VIIRS-observed water fractions [30] and constructed the regression models (see Section 4.1) using USGS in situ streamflow data. NWM streamflow forecasts served as inputs to generate the pseudo-forecasts of FIER water fraction, which were validated against the concurrently observed water fractions. Forecasted FIER water fractions thereby function as indicators of flood signals, with higher fractions indicating increased water concentration and potential flooding.

Finally, given that flooding was ranked as the second most abiotic stressor (after drought) contributing to crop production losses [31], we demonstrated a potential agricultural application of FIER water fraction forecasts. This application, alongside other flood risk management resources, can partly assist farmers in proactively mitigating forthcoming flood damage.

2. Study Regions

The RRNB, a remnant of the glacial lake Agassiz in the late Pleistocene, is one of the flattest areas in the world [32,33]. Flooding events here usually occur in late spring and early summer due to increased streamflow from snowmelt and rainfall. The area is highly vulnerable to flooding due to its flat terrain and the unique northward flow direction of the Red River of the North, which consistently receives meltwater and ice from the south, resulting in ice jams exacerbating flooding. In addition, the high clay content in RRNB soils impedes water movement, increasing flooding risk [34]. Our focus was on the flood-prone region in the RRNB, spanning from near Winnipeg, Canada, to Grand Forks, North Dakota, U.S. This region experienced severe flooding incidents in the years 2011, 2019, 2020, and 2022, with the 2022 flooding event considered the worst in a decade [35–37].

The Mississippi River Basin is the fourth largest drainage system in the world, draining about 41 percent of the CONterminous United States (CONUS) [38]. We focused on the flood-prone region extending from near Cairo, Illinois, to near Memphis, Tennessee, mostly in the Upper Mississippi Alluvial Plain (UMAP). Similarly to the RRNB, the impermeable soils and the flat terrains in the UMAP make the region susceptible to frequent flooding, primarily triggered by rainfall and snowmelt. Recent years have experienced unprecedented floods, some of the most significant in nearly a century. Notably, the 2011 and 2019 floods were attributed to heavy storm rainfall and late spring snowmelt [39,40]. The flooding in 2019 was even regarded as the longest-lasting flood in almost a century [41].

Figure 2 (left column) shows the historical maximum inundated extents and permanent water from 1984 to 2022, obtained from the Joint Research Center (JRC) of the European Commission [42], on the top of dark gray polygons outlining our study regions. Indeed, the historical maximum inundated extents (shown in light blue in Figure 2) represent the areas that have been frequently flooded over the 38-year period from 1984 to 2022. The inserts show their relative locations to the surrounding states. Despite flood susceptibility, the stream sediments make their soils highly fertile and suitable for agriculture [43]. Most of the lands in the regions are cultivated croplands according to the latest USGS land cover data, USGS National Land Cover Database (NLCD) 2021 [44], as shown in Figure 2 (right column).

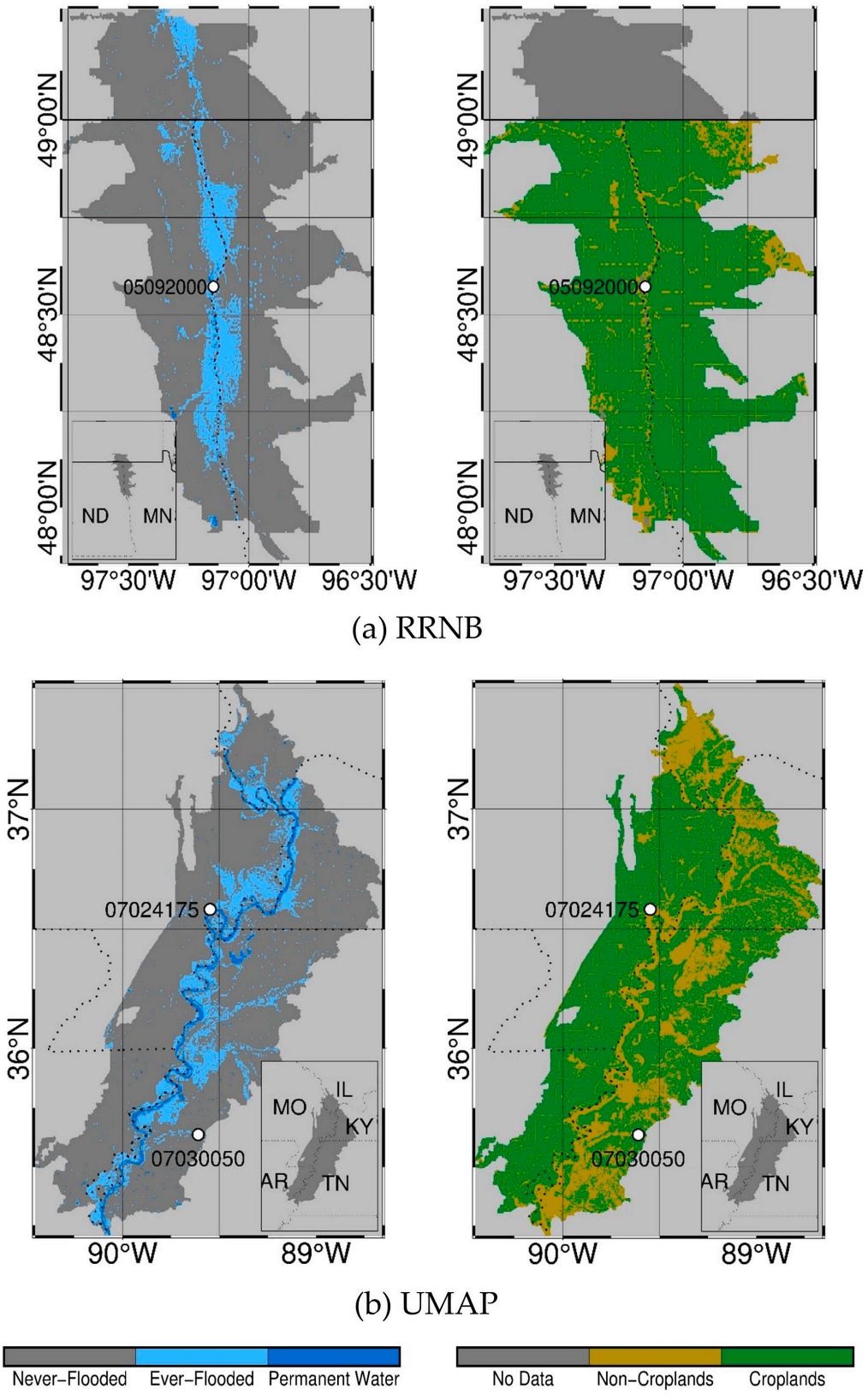

Figure 2. (**Left column**) JRC historical maximum inundation extents and permanent water from 1984 to 2022 [42], and (**right column**) the USGS NLCD 2021 cultivated croplands [44] in (**a**) RRNB and (**b**) UMAP. The white dots show the locations of the USGS in situ gauges used in this study.

3. Data

3.1. VIIRS-Observed Water Fractions

To apply FIER in water fraction forecasting, we extracted spatiotemporal patterns (see Section 4.1) depicting changes in water fraction from historical multi-temporal observations acquired by VIIRS. VIIRS provides images with a spatial resolution of 375 m and includes five spectral bands ranging from visible to thermal infrared channels. The VIIRS imagery is superior to the MODIS imagery in flood detection as it has a higher spatial resolution (375 m versus 500 m) in the short-wave infrared channel, crucial for flood detection and water fraction retrieval. Additionally, The VIIRS imagery offers a wider swath width and more consistent across-scan spatial resolution, ensuring more comprehensive global daily coverage and enhancing flood mapping quality [29,30].

We used the daily composite of 375 m resolution VIIRS-observed water fractions produced by the operational VIIRS global flood mapping system [29,30,45]. Since VIIRS is an optical sensor susceptible to cloud occlusion, we selected historical water fractions from 2012 to 2020 with less than 5% of cloud cover in the study regions to enable FIER to forecast cloud-free water fractions. The 5% threshold was set based on trial-and-error experiments. Increasing it resulted in the extraction of more flood-irrelevant spatiotemporal patterns, while decreasing it resulted in the exclusion of VIIRS water fraction data acquired during peak flows, where the presence of minimal cloud extent is inevitable. This process resulted in 1014 images for RRNB and 827 images for UMAP. To fill the cloud gaps, spatial interpolation was applied. First, valid pixels (non-cloud pixels) near the gaps (cloud pixels) were identified. Then, a radial search was performed, expanding outward until adequate neighboring pixels were found within a specified distance. The missing data were then filled in by considering the influence of these pixels, giving more weight to those that are closer, resulting in a seamless and consistent interpolation process. Finally, the spatiotemporal patterns were extracted from these images.

3.2. USGS In Situ Streamflow Data

To identify flood-relevant spatiotemporal patterns associated with streamflow variations, we used in situ streamflow data from USGS National Water Information System (NWIS) (https://maps.waterdata.usgs.gov/mapper/index.html (accessed on 17 September 2024)). These patterns were extracted from the historical VIIRS-observed water fractions and used to build regression models, which will be explained in more detail in Section 4.1, correlating them with streamflow variations. The USGS NWIS currently provides updated data at 10,977 sites across the entire U.S. For this study, we selected the gauges where streamflow data exhibited a Pearson correlation coefficient (CC) > 0.5 with the temporal patterns extracted from the VIIRS-observed water fractions. CC was used as the selection criterion since it is a straightforward statistic that reduces process complexity and computational burden, facilitating FIER implementation for larger areas.

In addition, we have ingested streamflow data into FIER as an effective flood indicator, and selected flood-relevant temporal modes based on the correlation analysis, which showed satisfactory results (i.e., FIER-forecasted water fraction maps), making the use of other statistics unnecessary. Setting 0.5 as the correlation threshold is a trade-off between including more flood-relevant modes (by not setting the threshold too low) and avoiding the exclusion of significant modes (by not setting threshold too high). After applying the correlation analysis, one gauge (for RRNB) and two gauges (for UMAP) were selected among all USGS gauges within the regions of interest. The locations of the selected gauges are shown as white dots in Figure 2, with detailed information provided in Table 1.

Table 1. Details of the selected USGS streamflow gauges and corresponding NWM reach IDs.

Study Area			RRNB	UMAP
FIER framework building	USGS	Gauge ID	05092000	07024175 07030050
		Gauge name	Red River of the North at Drayton, North Dakota	Mississippi River at New Madrid, Missouri Hatchie River at Rialto, Tennessee
Input data for FIER forecasting	NWM reach ID		7077522	7469392 14073444

3.3. NWM Streamflow Forecasts

We used the NWM streamflow forecasts [46], at the reaches where the selected USGS streamflow gauges are located (see Table 1), as inputs to the FIER framework to forecast water fractions. The NWM, launched by NOAA in 2016, is a hydrologic modeling framework that provides operational streamflow forecasts with various lead times at approximately 2.7 million river reaches throughout the U.S., encompassing the entire CONUS, Puerto Rico, Hawaii, and the Virgin Islands. The core of the NWM is the Weather Research and Forecasting hydrologic model (WRF-Hydro), which uses meteorological forcing data from various sources depending on the region and the temporal range of the forecasts. WRF-Hydro employs the Noah-MP Land Surface Model (LSM) to simulate land surface processes. Separate water routing modules perform diffusive wave surface routing and saturated subsurface flow routing on a 250 m grid, along with Muskingum–Cunge channel routing to the water drainage network, based on the National Hydrography Dataset [22,46].

The two study regions are both located within the CONUS, where the NWM provides hourly short-range forecasts, and 6-hourly medium- and long-range forecasts. Given their longer lead times (up to about a week for medium-range and a month for long-range), we used the medium- and long-range forecasts for this study instead of the short-range forecasts (up to 18 h). The medium- and long-range forecasts are forced with meteorological outputs from the Global Forecasting System (GFS) and Climate Forecast System (CFS), respectively, and are produced as ensemble forecasts. We calculated the daily averages of medium- and long-range forecasts issued at 00:00 am for all the available ensembles, with lead times of up to 8 days and 30 days, respectively, serving as inputs for FIER to generate water fraction forecasts. Using daily averaged NWM forecasts provides a broad representation of daily hydrological conditions while avoiding the complexities of managing uncertainties in individual ensemble forecasts.

3.4. Land Cover and Crop-Relevant Data

To demonstrate the potential application of FIER water fractions in agriculture, it is important to understand the crop calendar in the study regions. This information provides insights into whether floods could pose a threat to crop growth. Considering the varied calendars of different crops, we looked into the United States Department of Agriculture (USDA) Cropland Data Layer (CDL) for the years 2021 and 2022. The predominant crops in the RRNB and UMAP were found to be spring wheat and soybeans, respectively, covering about 30 to 40% of the study areas (see Figure 3). According to the crop calendar in the USDA Country Summary [47], the planting periods for spring wheat and soybeans span from April to May, and May to June, respectively.

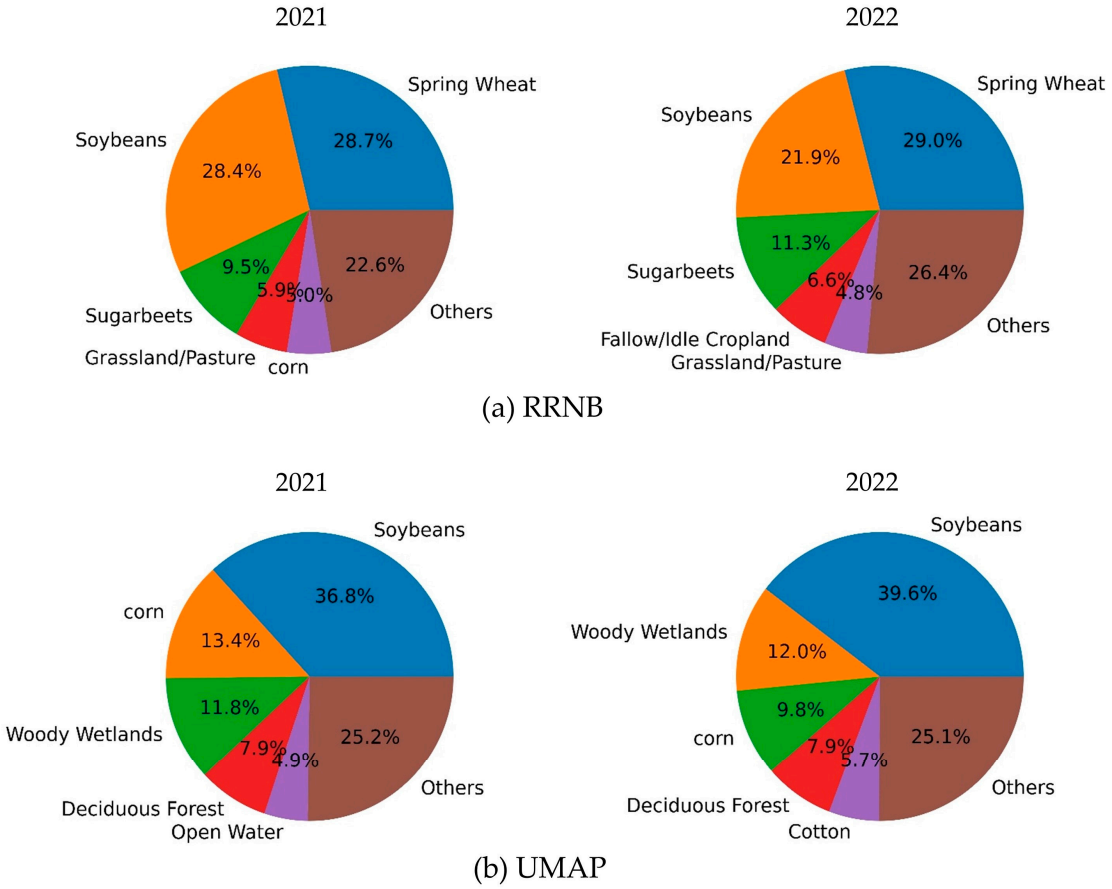

Figure 3. Pie charts of the top five classes in the USDA CDL for 2021 and 2022 in the (**a**) RRNB and (**b**) UMAP, showing the most dominant crops are spring wheat and soybeans, respectively.

4. Method

4.1. Overview of FIER

FIER, a data-driven framework, synthesizes future flood signals from satellite images based on the relationship between the observed historical floods and hydrological data. It first decomposes the historical multi-temporal satellite images into several significant modes of spatial and temporal patterns using the Rotated Empirical Orthogonal Function (REOF) analysis, a Principal Component Analysis (PCA) approach [48], and the Monte Carlo significant test [49]. The extracted temporal patterns are called Rotated Temporal Principal Components (RTPCs), and the extracted static spatial patterns are called Rotated Spatial Modes (RSMs), labeled as RSM-01 (RTPC-01) for the first mode, RSM-02 (RTPC-02) for the second mode, and so forth. We have set 99% as the variance threshold, meaning that PCA selects the smallest number of components (in this case, spatial and temporal modes) needed to capture 99% of the total variance in the data.

Next, a correlation analysis is performed between each mode of RTPCs and hydrological data. Each RTPC mode is paired with its most strongly correlated hydrological data using a neural network regression model, chosen for its flexibility in fitting function [50]. The optimal models are automatically determined via grid search with K-fold cross-validation to prevent overfitting [51]. The regression models are trained using in situ observations (USGS streamflow) to ensure the trained model used for synthesis in the next step is not affected by the inherent uncertainties/biases in hydrological model outputs (i.e., simulated streamflow).

Flood-related modes are selected based on their fitted regression models, with a Nash–Sutcliffe Efficiency (NSE) higher than 0.6. NSE penalizes overestimation or underestimation in simulations, making it particularly useful in hydrology, where capturing both the mag-

nitude and trend of streamflow or precipitation is crucial. The forecasted hydrological data are then input into the trained regression models to estimate future RTPCs, representing future flood-relevant temporal patterns. Finally, future flood signals are synthesized by summing the product of each mode of forecasted RTPCs and RSMs, similarly to the "synthesis process" in PCA. Figure 4 summarizes the FIER process, with further details available in Chang et al. [25,26].

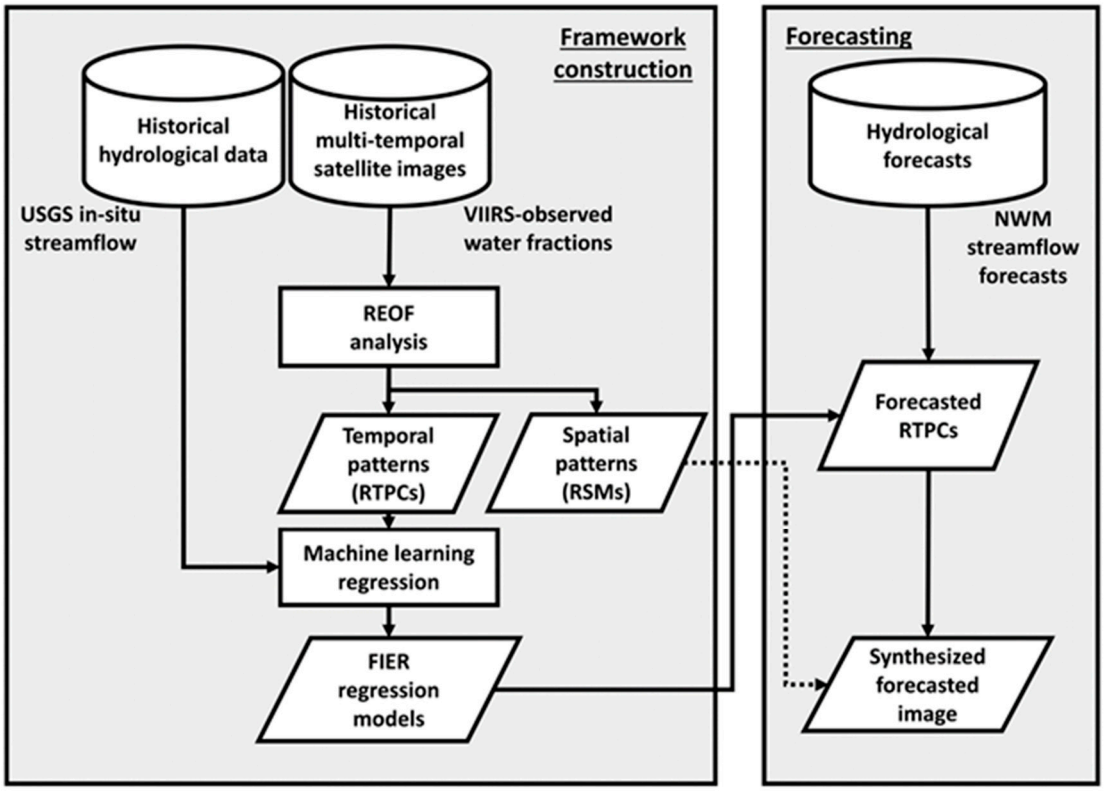

Figure 4. Flowchart of the FIER process largely consists of framework construction and forecasting. Dashed line arrow indicates the synthesis of RSMs and forecasted RTPCs.

4.2. FIER Water Fraction Forecasting

To forecast water fraction, historical VIIRS-observed water fractions were first decomposed by the REOF analysis. Then, we used the USGS in situ streamflow data to identify the flood-relevant modes and build the regression models. These models were then fed with streamflow forecasts from NWM to estimate future RTPCs, which were combined with corresponding RSMs to synthesize future water fractions. However, since only modes correlated with the hydrological data (i.e., the in situ streamflow data from USGS) were used for synthesizing water fractions through FIER, the synthesized water fraction did not maintain their original scale of 0 to 100%. To address this, we applied quantile mapping, a common bias correction method, to restore the water fractions as accurately as possible [52,53]. This method aligns model estimations with observations by matching quantiles. The quantile mapping was conducted pixel by pixel across the study areas. For each pixel, Cumulative Distribution Functions (CDFs) were created for both historical FIER-synthesized water fractions (using historical USGS in situ streamflow) and VIIRS-observed water fractions. These CDFs allowed us to convert water fraction values into quantiles. Utilizing these CDFs, the quantiles of FIER-synthesized water fraction forecasts were determined. Then, the VIIRS-observed water fractions corresponding to the same quantiles were used as the "corrected" FIER-synthesized water fraction forecasts. Figure 5 summarizes this quantile mapping process.

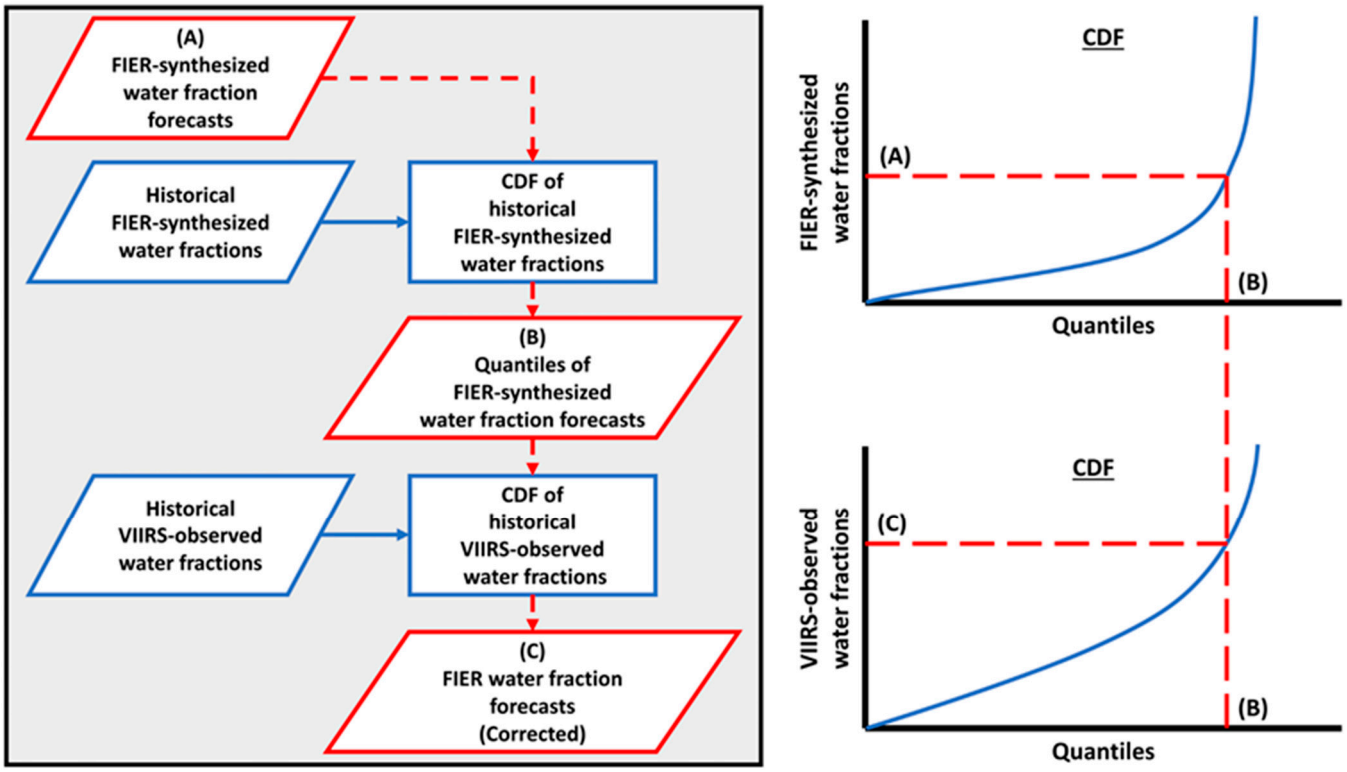

Figure 5. Flowchart (**left**) and schematic view (**right**) of the quantile mapping process employed to correct the biases in FIER water fraction forecasts. The blue boxes in the flowchart represent historical water fraction data (FIER-synthesized and VIIRS-observed) and their respective CDFs. The red boxes in the flowchart represent forecasted water fraction data and the corresponding extracted quantiles.

5. Results and Discussion

5.1. Flood-Relevant Spatiotemporal Patterns and FIER Regression Models

Figures 6 and 7 show (a) streamflow-related RSMs, (b) corresponding RTPCs along with USGS in situ streamflow data, and (c) the neural network regression models in the RRNB and UMAP, respectively. In the RSMs, the reddish pixels represent the flooded areas observed by VIIRS. It is expected that as the streamflow data (and consequently RTPCs) increase, the FIER water fraction forecasts in these reddish areas will exhibit higher values. Additionally, the distribution of these reddish pixels aligns closely with the historical maximum inundation extents shown in Figure 2a.

The Monte Carlo test identified six significant modes in the RRNB. Among these, mode-01 and mode-02 were selected based on the correlation coefficient criteria and subsequently coupled with USGS in situ streamflow data at gauge 05092000, located in the mainstem of the Red River of the North. In the UMAP analysis, eight significant modes were identified, and mode-01, mode-02, mode-04, and mode-05, which met the correlation threshold, were selected. Mode-01, mode-02, and mode-04 were coupled with USGS in situ streamflow data at gauge 07024175 in the Mississippi River mainstem, while mode-05 was coupled with in situ streamflow data at USGS in situ gauge 07030050 in a Mississippi River tributary. The choice of the gauges is justified by the alignment of reddish pixels distributions in the RSMs with the river reaches where these gauges are located (see Figures 6a and 7a). Then, the gauge with the highest correlation to RTPCs was chosen to build the regression model. The neural network regression models exhibited high quality, with Nash–Sutcliffe Efficiency (NSE) ranging from 0.6 to 0.95 (see Figures 6c and 7c). Table 2 presents the structures of the neural network regression models.

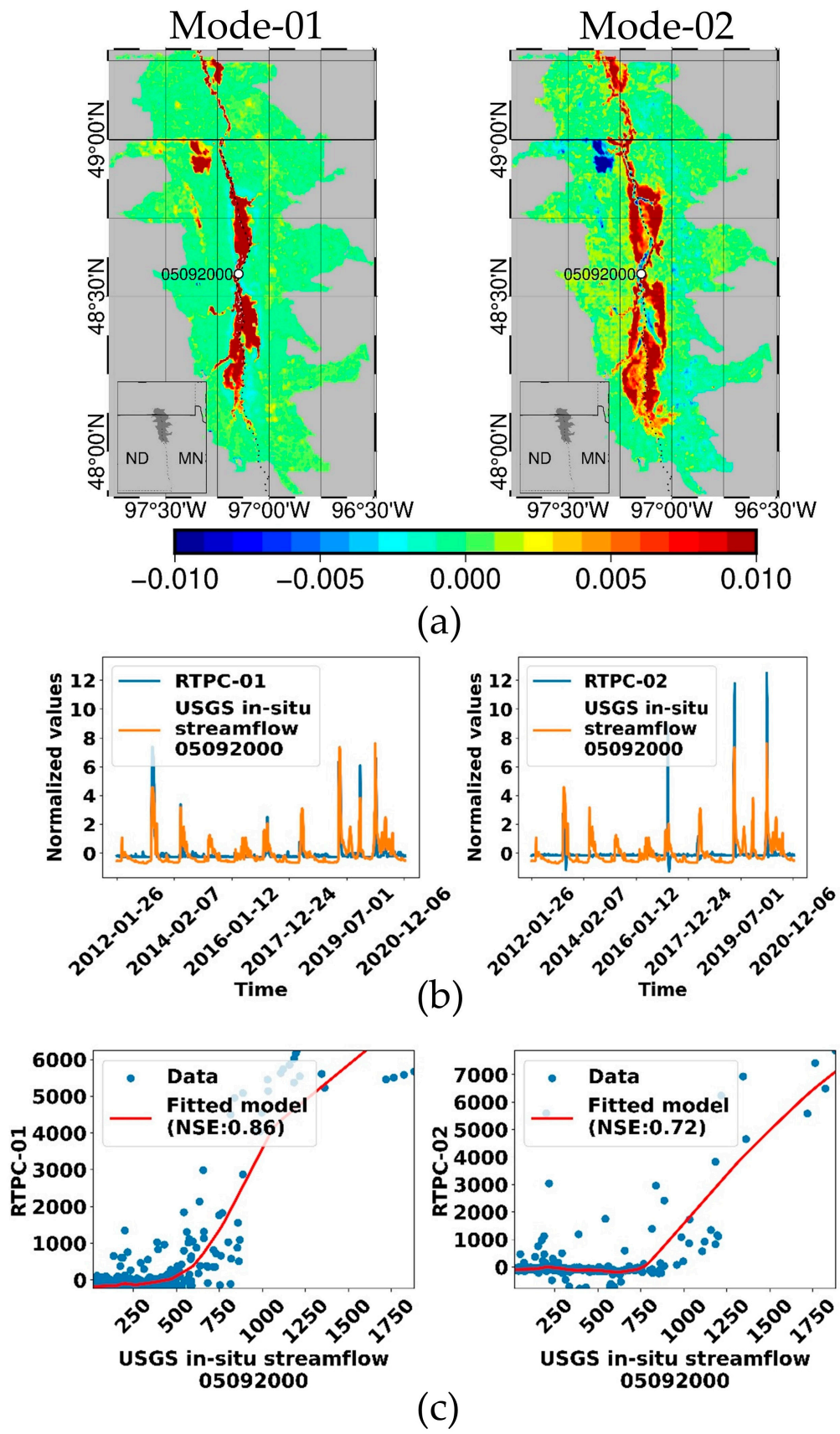

Figure 6. The extracted streamflow-related (**a**) RSMs, (**b**) RTPCs along with USGS in situ streamflow data, and (**c**) neural network regression models for FIER water fraction forecasting in the RRNB.

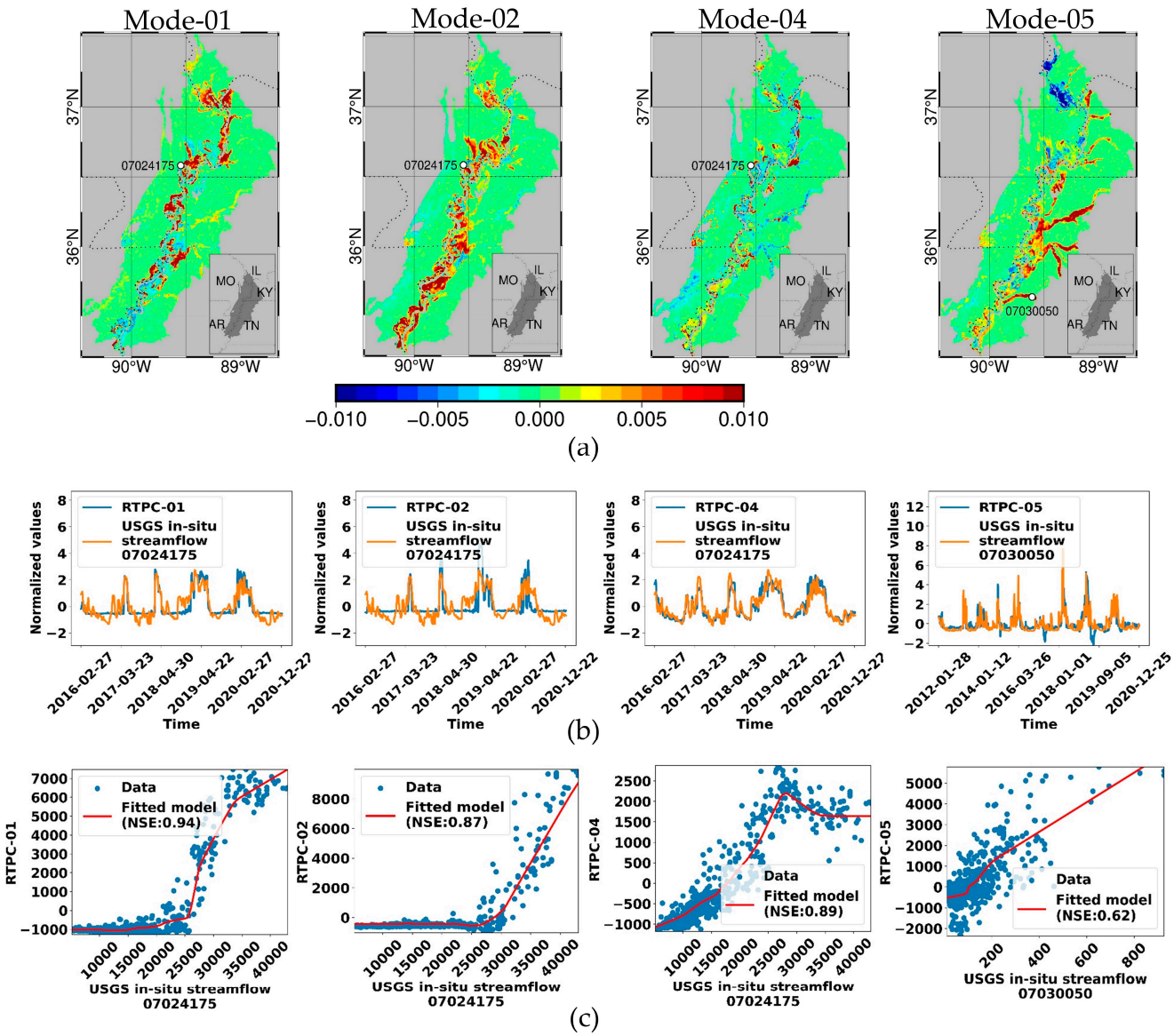

Figure 7. The extracted streamflow-related (**a**) RSMs, (**b**) RTPCs along with USGS in situ streamflow data, and (**c**) neural network regression models for FIER water fraction forecasting in the UMAP.

Table 2. Structures of the fitted neural network regression models of each streamflow-related mode for FIER water fraction forecasting in the RRNB and UMAP along with corresponding selected gauges and NSEs.

Streamflow-Related Mode	Selected Input USGS In Situ Gauge	Number of Hidden Layers	Number of Neurons in Each Hidden Layer	NSE
		RRNB		
Mode-01	05092000	4	15	0.86
Mode-02	05092000	4	30	0.72
		UMAP		
Mode-01	07024175	5	45	0.94
Mode-02	07024175	3	45	0.87
Mode-04	07024175	5	20	0.89
Mode-05	07030050	5	50	0.62

To demonstrate the advantage of using daily VIIRS water fractions over the Sentinel-1 dataset (used in previous FIER efforts), we compared the performance of Sentinel-1-based FIER by replicating the processes applied to VIIRS water fractions. This included comparing extracted RTPCs, RSMs, and the skills of the corresponding regression models. For Sentinel-1 inundation extent forecasting, we extracted streamflow-related spatiotemporal patterns from historical multi-temporal Sentinel-1 VV-polarized Ground Range Detection High-resolution (GRDH) intensity imagery. The VV-polarization was chosen considering its superior surface water mapping capabilities [54,55]. Sentinel-1A images acquired on high-streamflow dates from 2021 to 2022 were used to generate observed inundation extents for evaluating FIER forecast accuracy. In the RRNB, streamflow at selected gauges above the 95th percentile from 2012 to 2020 was considered high, providing eight reference images. However, only one reference image met the 95th percentile standard in UMAP. Thus, we adjusted the high-streamflow standard threshold to the 80th percentile, yielding 13 reference images. To manage the computational demands of Sentinel-1 imagery retrieval and preprocessing, we leveraged the publicly available cloud-based Google Earth Engine (GEE) data catalog and GEE-based Application Programming Interface (API). The Hydrologic Remote Sensing Analysis for Floods (HYDRAFloods), a GEE API-based, open-source Python application (https://servir-mekong.github.io/hydra-floods/ (accessed on 17 September 2024)), developed by the NASA SERVIR Coordination Office (SCO), was used for image mosaicking, slope correction [56] using the Multi-Error-Removed Improved-Terrain Digital Elevation Model (MERIT DEM) [57], and the Gamma-Map speckle filtering [58]. The permanent water bodies were masked using the Joint Research Centre (JRC)'s Global Surface Water Data [42] to account for SAR intensity variations caused by winds. The preprocessed images were exported as GeoTIFFs with a 30 m spatial resolution, from which the spatiotemporal patterns were extracted. FIER Sentinel-1 inundation extent forecasts also maintain this 30 m spatial resolution.

Figures 8 and 9 show the extracted streamflow-related (a) RSMs, (b) corresponding RTPCs along with USGS in situ streamflow data, and (c) the neural network regression models in RRNB and UMAP, respectively. In these RSMs, bluish pixels indicate flooded areas observed in the historical Sentinel-1 SAR intensity images. Thus, the FIER-synthesized SAR-like intensities in these areas will decrease with higher RTPCs (and streamflow), reflecting the lower intensities in the synthesized SAR-like images due to specular reflectance over flooded regions. This pattern is consistent with the historical maximum inundation extents shown in Figure 2.

In RRNB, mode-04, mode-07, and mode-08 were selected and coupled with USGS in situ streamflow data at gauge 05092000 on the Red River mainstem. In UMAP, mode-01 and mode-05 were selected and coupled with data from gauge 07024175 on the Mississippi River mainstem, while mode-04 was coupled with data from gauge 07026040 in the Mississippi River tributaries. The selection of gauges is justified as the bluish pixels in these RSMs are mostly distributed along the river reaches where the selected gauges are located (see Figures 8a and 9a). The neural network regression models exhibit a wide range of NSEs from 0.35 to 0.9 (see Figures 8c and 9c). The relatively lower NSEs are likely due to the limited number of historical Sentinel-1 images available for peak-flow periods, which hinders the extraction of sufficient flood-relevant spatiotemporal patterns for effective coupling with streamflow data. Table 3 shows the structures of the neural network regression models. The low NSE values for Sentinel-1 FIER compared to VIIRS water fraction (see Tables 2 and 3) further confirms that the insufficient number of Sentinel-1 images during peak-flow periods, as shown in Figure 1, has significantly impacted the performance of FIER, emphasizing the advantage of employing VIIRS daily water fraction product.

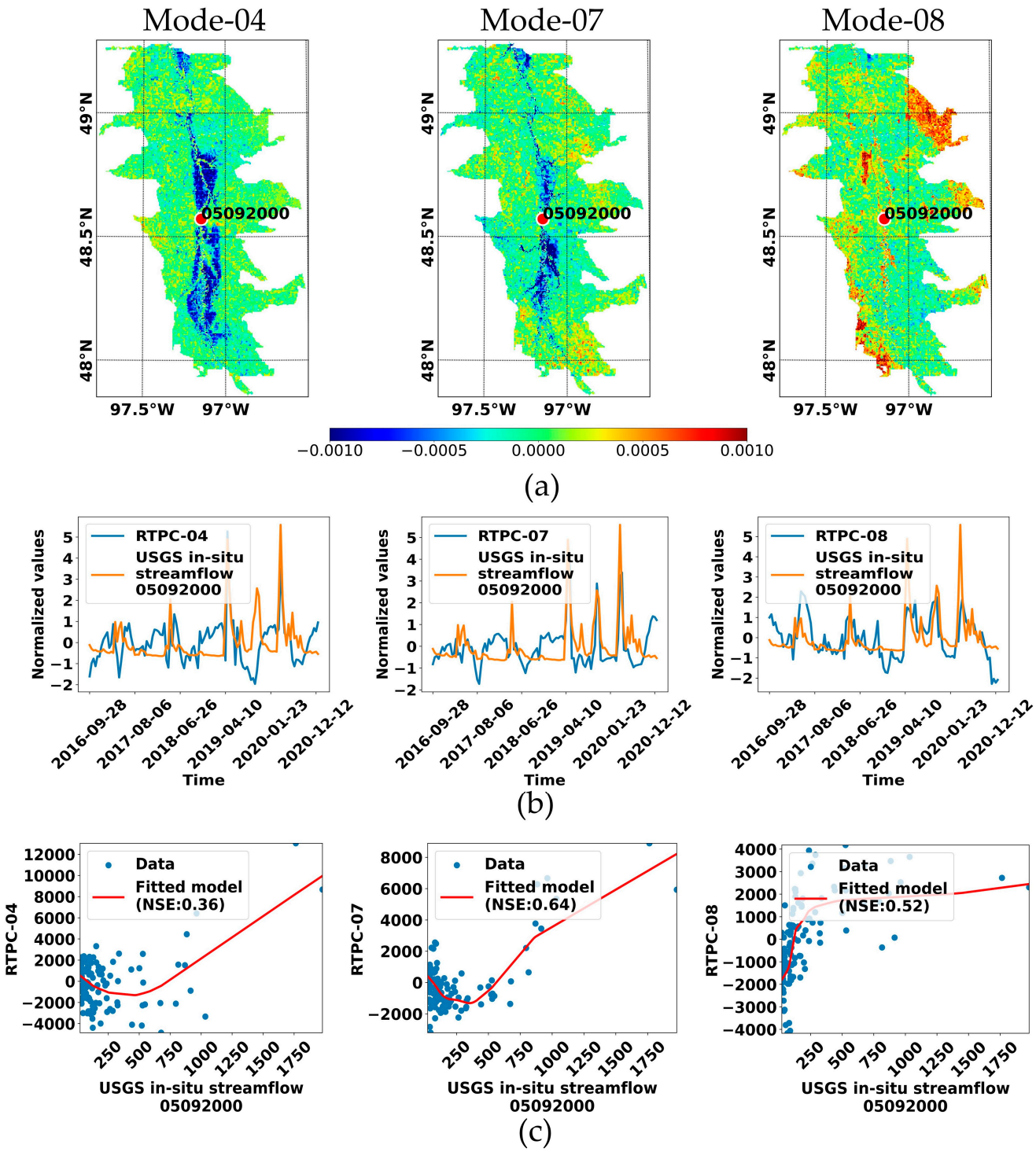

Figure 8. The extracted streamflow-related (**a**) RSMs, (**b**) RTPCs along with USGS in situ streamflow data, and (**c**) neural network regression models for FIER Sentinel-1 inundation extent forecasting in the RRNB.

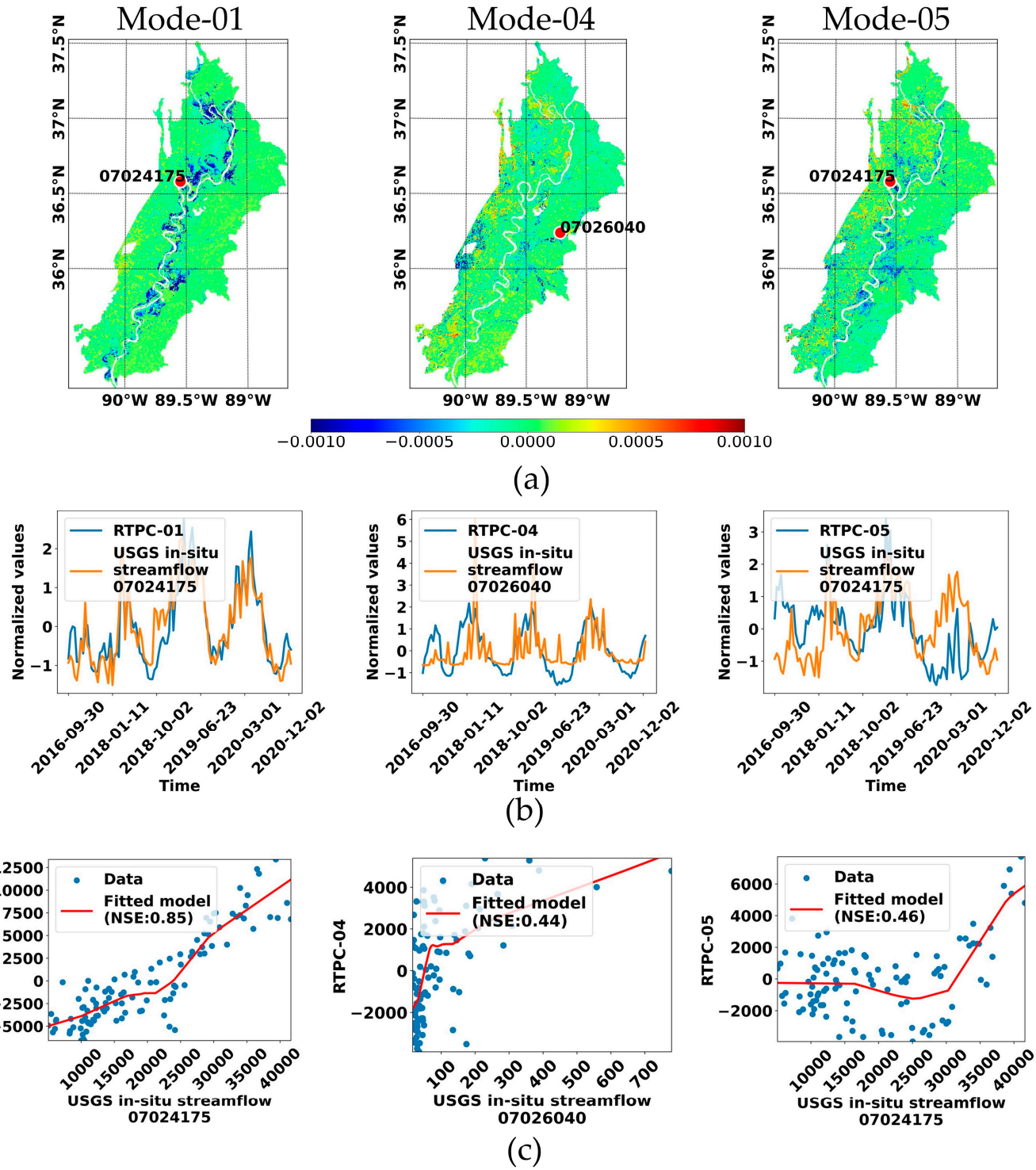

Figure 9. The extracted streamflow-related (**a**) RSMs, (**b**) RTPCs along with USGS in situ streamflow data, and (**c**) neural network regression models for FIER Sentinel-1 inundation extent forecasting in the UMAP.

Table 3. Structures of the fitted neural network regression models of each streamflow-related mode for FIER Sentinel-1 inundation extent forecasting in the RRNB and UMAP along with corresponding selected gauges and NSEs.

Streamflow-Related Mode	Selected Input USGS In Situ Gauge	Number of Hidden Layers	Number of Neurons in Each Hidden Layer	NSE
		RRNB		
Mode-04	05092000	1	45	0.36
Mode-07	05092000	5	20	0.64
Mode-08	05092000	5	50	0.52
		UMAP		
Mode-01	07024175	3	10	0.85
Mode-04	07026040	5	30	0.44
Mode-05	07024175	4	50	0.46

5.2. FIER Water Fraction Forecasts and Skill Evaluation

To evaluate the accuracy of the FIER water fraction forecasts, we generated pseudo-forecasts using the historical NWM medium-range (with 1- to 8-day lead times), and long-range (with 10-, 15-, 20-, 25-, and 30-day lead times) streamflow forecasts as the inputs. These are referred to as the FIER medium-range and long-range water fraction pseudo-forecasts, respectively. Additionally, we produced FIER water fraction pseudo-nowcasts using the USGS in situ streamflow data, representing the optimal results that FIER can produce when there are no errors in the input streamflow data. We used the skills of these pseudo-nowcasts as a baseline for evaluation.

We computed the absolute errors (AEs) of the FIER water fraction pseudo-nowcasts and pseudo-forecasts in historically flooded areas (excluding the permanent water bodies, see Figure 1) by comparing them with observed water fractions during high-streamflow (streamflow > 95th percentile of historical streamflow from 2012 to 2020) between January 2021 and August 2023. This analysis involved 95 images with 413,484 pixels in the RRNB and 48 images with 619,403 pixels in the UMAP. In both regions, AEs < 10%, 20%, and 30% accounted for approximately 62–68%, 68–73%, and 73–77% of the pixels for UMAP and RRNB, respectively, indicating that the skills of FIER medium-range pseudo-forecasts closely align with those of FIER pseudo-nowcasts (see Figure 10). However, FIER long-range pseudo-forecasts showed reduced accuracy, with AEs < 10%, 20%, and 30% covering around 58–61%, 61–62%, and 65–66% of the pixels for UMAP and RRNB, respectively (see Figure 8a).

Further analysis of over 100,000 pixels with high water fractions (water fraction > 80%) revealed that in FIER water fraction pseudo-nowcasts, about 61–82%, 75–88%, and 80–90% of these high-water fraction pixels have AEs < 10%, 20%, and 30%, respectively, in both UMAP and RRNB. This indicates that FIER performs better during peak-flow periods (water fraction > 80%) than in dry periods, highlighting that FIER is well suited for flood forecasting. Despite using USGS gauge station data to generate pseudo-nowcasts, NWM forecasts tend to be biased. Nevertheless, 70–80% of high water fraction pixels in FIER medium-range forecasts exhibit AEs of less than 30%, which is slightly lower than the skill of the FIER pseudo-nowcasts. However, the accuracy of FIER long-range pseudo-forecasts decreases, with only approximately 30–40% of high water fraction pixels showing AEs < 30% (see Figure 10b).

Since the FIER framework relies on NWM streamflow forecasts to generate the water fraction forecasts, errors in NWM streamflow forecasts can propagate into FIER water fraction forecasts. Table 4 shows the Relative Root Mean Squared Errors (RRMSEs) of NWM streamflow forecasts at selected river reaches on the high-streamflow dates, averaged across the lead times. The average RRMSEs of NWM long-range streamflow forecasts are about two to three times greater than those of NWM medium-range streamflow forecasts, contributing to the lower accuracy of FIER long-range water fraction pseudo-forecasts.

However, improving FIER forecast accuracy is possible by bias-correcting NWM streamflow forecasts, particularly long-range ones, using USGS in situ streamflow data before integrating them into the FIER framework.

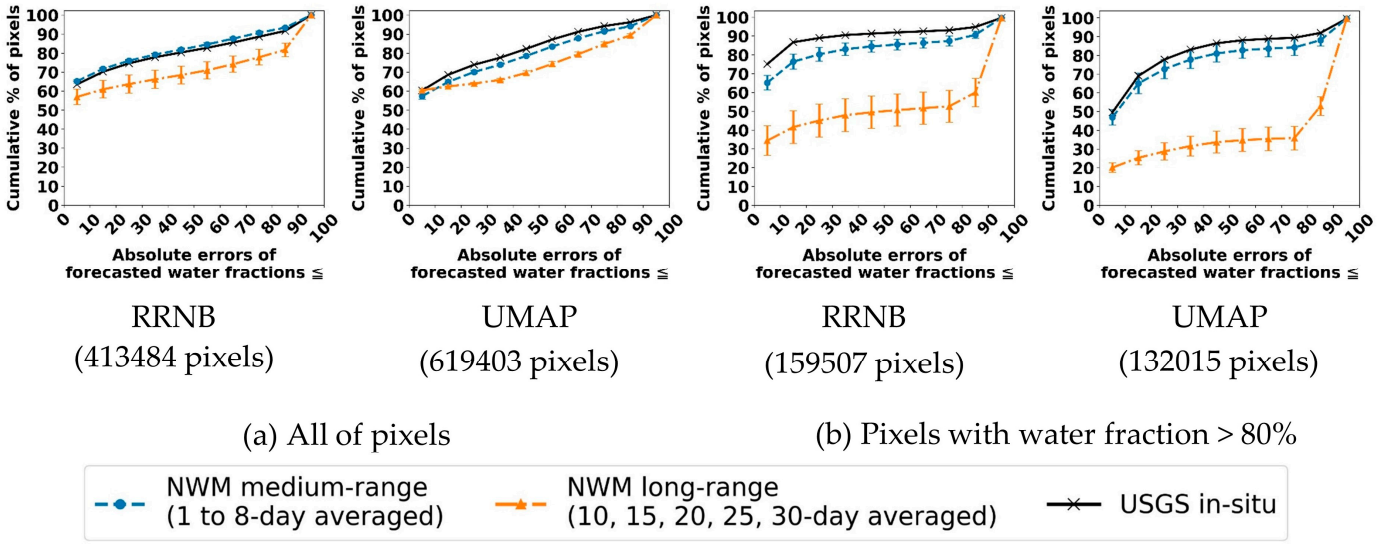

Figure 10. Cumulative percentages of pixels in different ranges of AEs in the RRNB and UMAP over (**a**) all pixels and (**b**) pixels with high water fractions (>80%).

Table 4. Averaged RRMSEs of the NWM medium-range and long-range forecasts over the lead times at the selected river reaches on the high-streamflow dates.

RRNB			UMAP		
NWM Reach ID	NWM Forecasting Range		NWM Reach ID	NWM Forecasting Range	
	Medium	Long		Medium	Long
7077522	2.24 ± 0.37 (%)	6.46 ± 0.72 (%)	7469392	2.73 ± 0.54 (%)	6.77 ± 0.87 (%)
---	---	---	14073444	6.92 ± 1.41 (%)	15.48 ± 0.75 (%)

Figure 11 compares the historical observed water fractions with FIER water fraction pseudo-nowcasts and 8-day FIER medium-range water fraction pseudo-forecasts on the highest streamflow dates in 2022 and 2023 in the RRNB. Results for 2021 in the RRNB are omitted due to the absence of flooding, as it was the driest year on record since 1885. The UMAP results for 2021, 2022, and 2023 are shown in Figure 10. Notably, FIER water fraction forecasts are cloud-free (Figures 11c and 12c), providing a comprehensive view of floodwater distribution in advance. Overall, FIER water fraction pseudo-nowcasts agree well with the historical observed water fractions. The 8-day FIER medium-range water fraction pseudo-forecasts also agree with the observed water fractions on the peak streamflow date of 2021 and 2022, though they display lower values than the observed water fractions on the peak streamflow date in 2023. This discrepancy may be due to errors in the 8-day NWM medium-range streamflow forecast, which could be improved through bias correction methods such as those proposed by Sanchez Lozano et al. [59], and the Stream Analysis for Bias Estimation and Reduction (SABER) method [60,61].

Furthermore, FIER, like other data-driven approaches, relies on the assumption that historical relationships will persist into the future. FIER uses REOF analysis to decompose historical flood inundation extent maps into spatial modes linked to specific hydrological variables, ensuring stable relationships for forecasting. However, unprecedented extreme events may bring in new spatial modes induced by different hydrologic phenomena, such as abnormal precipitation patterns or intense hurricane events. Although the current version of FIER cannot extrapolate the forecasts in the case of unobserved extreme events,

its highly adaptable framework allows for quick recalibration with data from new events, enabling the model to be responsive to evolving hydrological dynamics. Future work aims to enhance FIER's capabilities by simulating extreme events to broaden its training and improve forecasting under diverse flood scenarios.

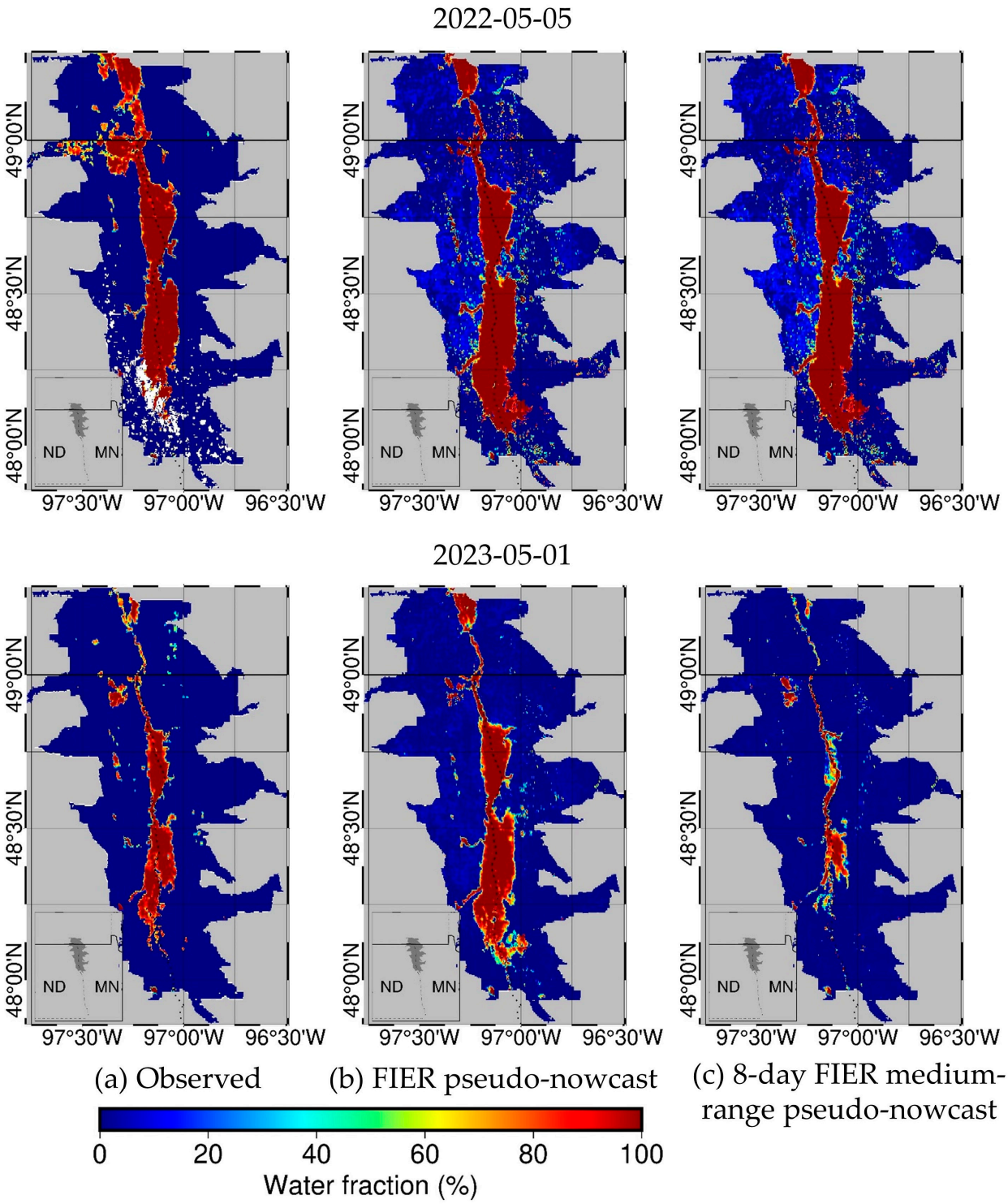

Figure 11. Water fractions on the peak-flood dates in 2022 and 2023 in the RRNB: (**a**) historical observation where white pixels are clouds, (**b**) FIER pseudo-nowcast, and (**c**) 8-day FIER medium-range pseudo-forecast.

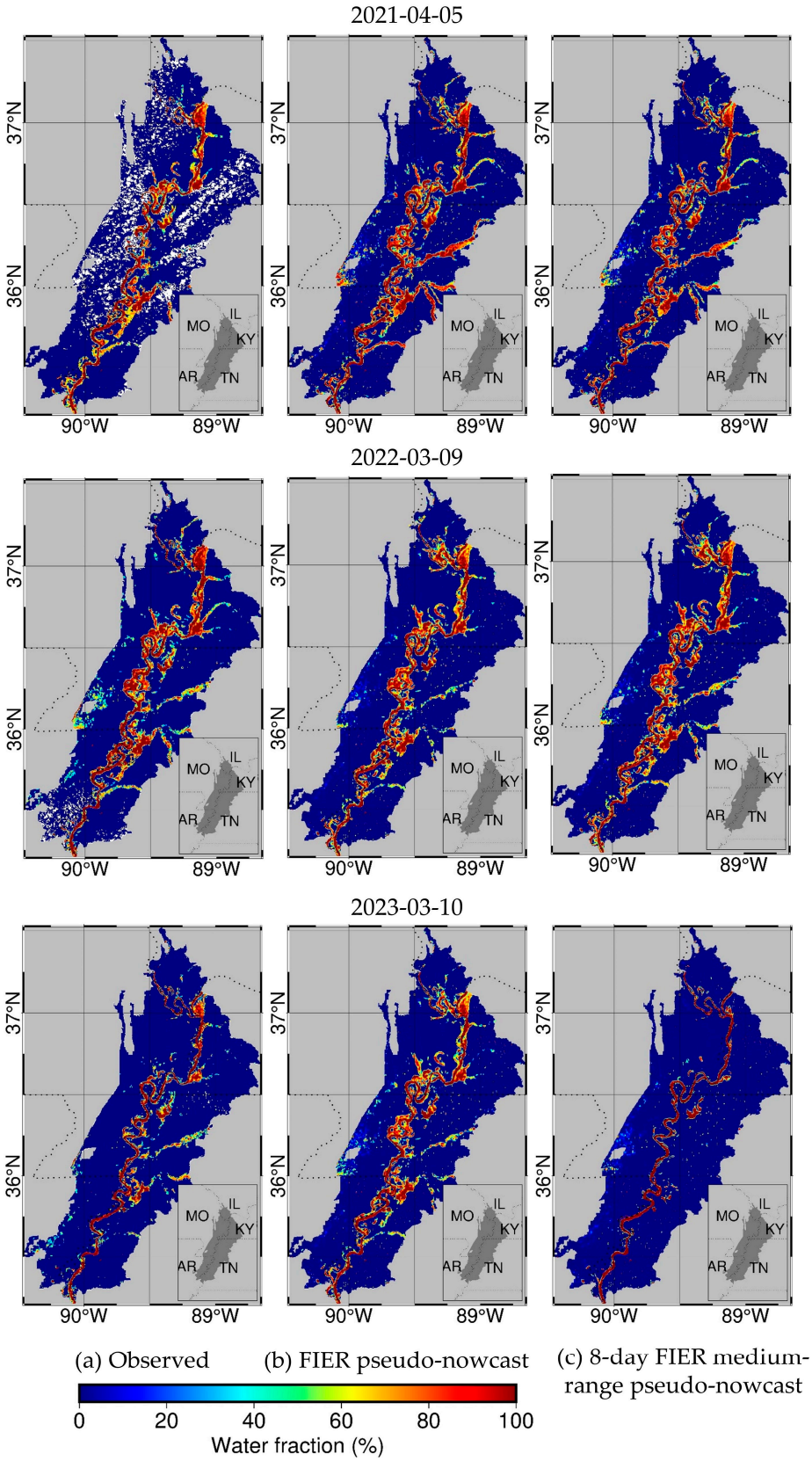

Figure 12. Water fractions on the peak flood dates in 2021, 2022, and 2023 in the UMAP: (**a**) historical observation where white pixels are clouds, (**b**) FIER pseudo-nowcast, and (**c**) 8-day FIER medium-range pseudo-forecast.

To more comprehensively assess the performance of FIER, we used three additional accuracy criteria: Cross Entropy (CE) [62], Fractions Skill Score (FSS) [63], and Structural Similarity Index (SSI) [64] for each flooding event in both study areas, as shown in Figures 11 and 12. *CE* quantifies the difference between the observed and forecasted probability distributions by considering each pixel's water fraction percentage as a probability. *CE* ranges from 0 (indicating a perfect match) to $+\infty$ (indicating a complete mismatch). In contrast, FSS and SSI both measure the spatial similarity between the observed and forecasted water fractions: FSS ranges from 0 (lowest spatial match) to 1 (highest spatial match), while SSI ranges from -1 (lowest similarity) to +1 (highest similarity). The accuracy metrics are calculated using the following formulas:

$$CE = -\frac{1}{N}\sum_{i=1}^{N}(O_i.\log F_i + (1-O_i).(1-\log(1-F_i))) \quad (1)$$

$$FSS = 1 - \frac{\sum_{i=1}^{N}(F_i - O_i)^2}{\sum_{i=1}^{N}\left({F_i}^2 + {O_i}^2\right)} \quad (2)$$

$$SSI(F,O) = \frac{(2\mu_F\mu_O + C_1)(2\sigma_{FO} + C_2)}{\left(\mu_F^2 + \mu_O^2 + C_1\right)\left(\sigma_F^2 + \sigma_O^2 + C_2\right)} \quad (3)$$

where O_i, F_i, and N represent the observed water fraction from VIIRS for the i-th pixel, the forecasted water fraction by FIER for the i-th pixel, and the total number of pixels, respectively. Additionally, μ_F, μ_O, σ_F^2, σ_O^2, and σ_{FO} denote the mean of the forecasted water fraction, the mean of the observed water fraction, the variance of the forecasted water fraction, the variance of the observed water fraction, and the covariance between the observed and forecasted water fractions, respectively. Constants C_1 and C_2 are used to stabilize the formula when denominators are small, set at 0.01 and 0.03, respectively. The evaluation metrics of FIER for the peak flood samples in the RRNB and UMAP (shown in Figures 11 and 12) are summarized in Table 5. Although FIER's overall performance in peak-flooding events is satisfactory, the inherent bias of the 8-day medium range NWM forecast led to lower FSS and SSI scores and higher *CE* values compared with the FIER pseudo-nowcast, particularly on 10 March 2023 in the UMAP and 1 May 2023 in the RRNB. Moreover, it should be noted that *CE* penalizes discrepancies between the water fraction values of the observations and forecasts while FSS and SSI both emphasize spatial alignment. Consequently, for example, in the UMAP, the FIER-synthesized water fraction with the lowest *CE* does not necessarily exhibit the most accurate spatial pattern (i.e., highest FSS and SSI).

Table 5. Quantitative accuracy assessment for each flooding event shown in Figures 11 and 12 for UMAP and RRNB.

		FIER Pseudo-Nowcast			**8-Day FIER Medium-Range Pseudo-Forecast**		
Study Area	**Date**	**CE**	**FSS**	**SSI**	**CE**	**FSS**	**SSI**
UMAP	2021-04-05	0.88	0.78	0.75	0.86	0.79	0.79
	2022-03-09	0.84	0.83	0.83	0.74	0.84	0.84
	2023-03-10	0.63	0.75	0.73	1.06	0.71	0.71
RRNB	2022-05-05	1.20	0.79	0.74	1.21	0.79	0.73
	2023-05-01	0.60	0.76	0.71	0.81	0.66	0.66

5.3. Showcaing the Potential of Flood Warning in Agriculture Using FIER

Nitrogen is typically the most limiting nutrient for crops, while oxygen is essential for the respiration process [65]. However, flooding can cause soil waterlogging, diminishing soil nitrogen contents and creating hypoxic (oxygen-deficient) or anoxic (oxygen-absent) conditions [66]. When soil becomes waterlogged, nitrogen is easily lost due to denitrification, nitrate leaching, and runoff [66], along with reduced soil nitrogen mineralization

rates [67]. Moreover, oxygen availability could be limited to near the soil surface due to hindered diffusion in water-filled pores, which negatively affects crop growth and production yields [66,68].

Fortunately, the application of "enhanced efficiency fertilizers" can aid crops in surviving soil waterlogging by controlling the nitrogen release rate and reducing nitrogen losses [66,69]. Recent studies have shown that these fertilizers reduce nitrogen losses and increase crop yields during wet years and in saturated soil conditions [70]. Additionally, slow-release solid oxygen fertilizers (e.g., CaO_2 and MgO_2) applied to flooded soils can alleviate hypoxic stress in the root zone and enhance crop yields [71,72].

One potential application of FIER water fraction forecasts is advising farmers on when and where to apply fertilizers to mitigate crop yield losses caused by forthcoming floods. Spring wheat and soybeans are the dominant crops in the RRNB and UMAP with planting periods from April to May and May to June, respectively (see Section 3.4). Figures 13 and 14 illustrate the average FIER medium-range water fraction pseudo-forecasts for the next 1 to 8 days in the fields of these dominant crops in the RRNB and the UMAP, respectively. These forecasts could have been generated before the peak flood during the planting periods. With this information, farmers could anticipate the timing and location of potential crop flooding, enabling more precise and cost-effective fertilizer application. This could help farmers decide whether to apply fertilizers, or delay planting in fields expected to be flooded or have higher water fractions in the coming days.

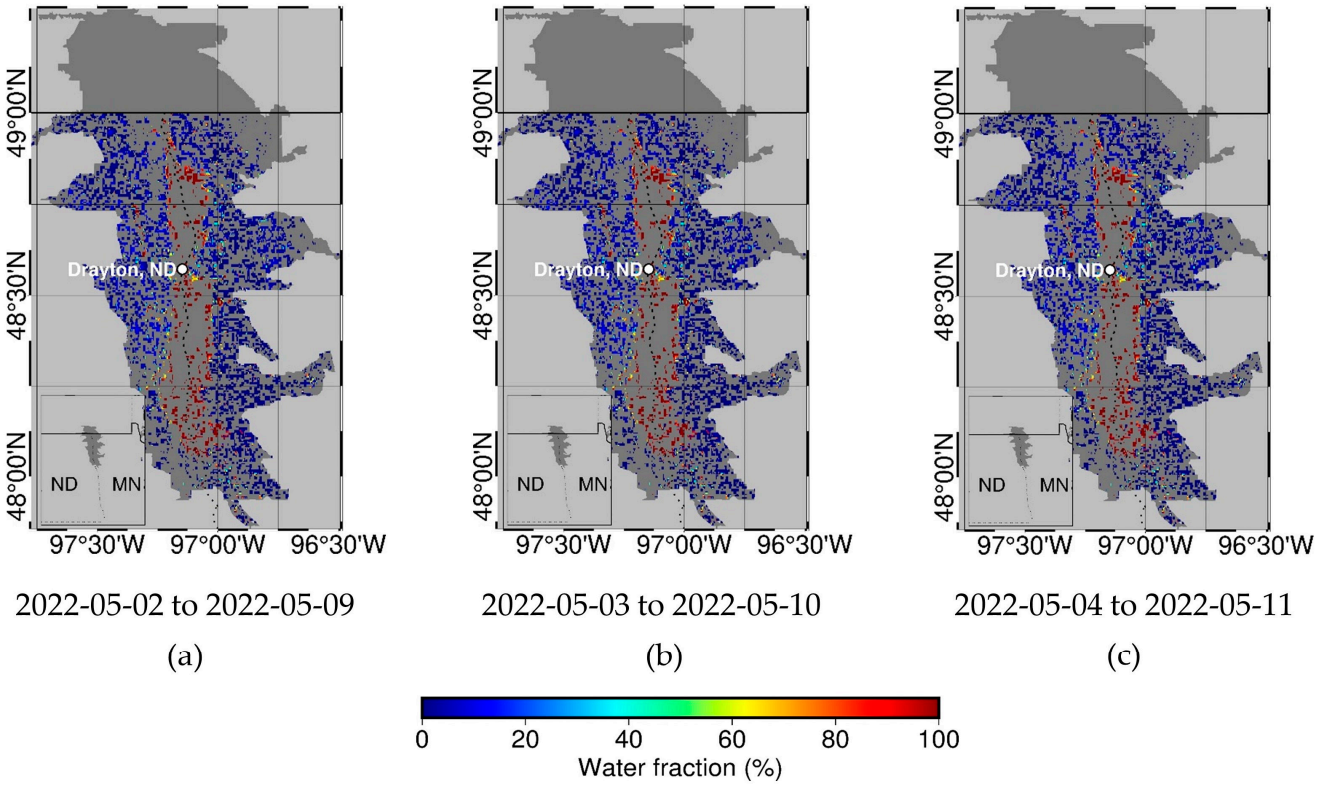

Figure 13. Examples of averaged FIER medium-range water fraction pseudo-forecasts over the next 1 to 8 days in the 2022 spring wheat fields in the RRNB, which could have been generated on (**a**) 2022-05-02, (**b**) 2022-05-03, or (**c**) 2022-05-04, before the peak flood on 2022-05-05 in the planting period.

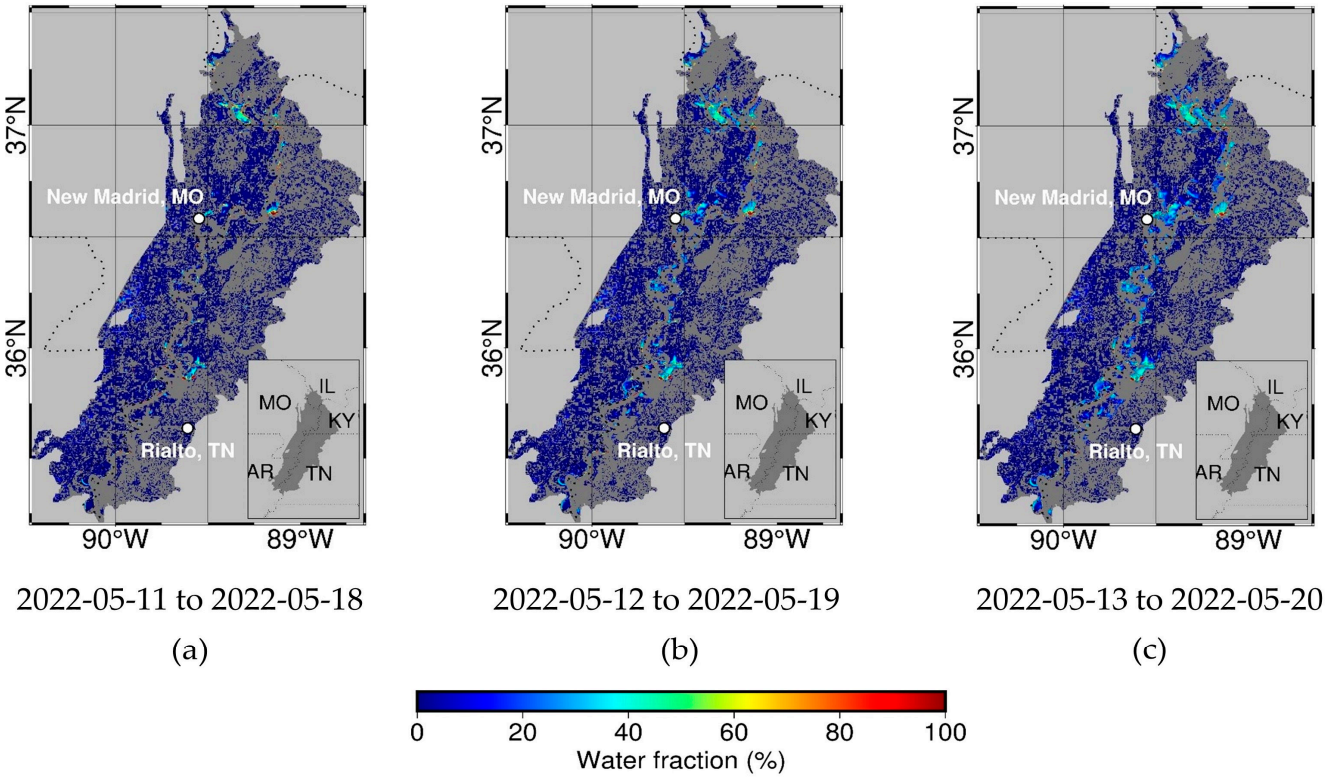

Figure 14. Examples of averaged FIER medium-range water fraction pseudo-forecasts over the next 1 to 8 days in the 2022 soybean fields in the UMAP, which could have been generated on (**a**) 2022-05-11, (**b**) 2022-05-12, or (**c**) 2022-05-13, before the peak flood on 2022-05-14 in the planting period.

6. Conclusions

Despite the growing need for real-time flood inundation forecasting, traditional methods like hydrodynamic modeling and HAND approaches face challenges in the U.S. due to computational burden and data accessibility issues. This study introduces FIER, a data-driven rapid flood inundation forecasting framework, which, for the first time, uses VIIRS optical sensor-derived water fractions and the NWM streamflow forecasts in flood-prone regions in the U.S., specifically the RRNB (Red River of the North Basin) and UMAP (Upper Mississippi Alluvial Plain), where inundation forecasting services are currently lacking. By utilizing the daily VIIRS water fraction product, FIER benefits from more historical data captured during their relatively shorter peak flow periods. In contrast, Sentinle-1 does not provide a sufficient number of observations.

In this study, FIER utilizes the NWM medium-range and long-range streamflow forecasts to produce water fraction forecasts with lead times of up to 8 and 30 days, respectively. We assessed FIER's performance by comparing its forecasts with historical observed VIIRS water fractions. The results show that FIER's accuracy is comparable to previous studies for nowcasts, with approximately 90% of high water fraction pixels exhibiting AEs < 30%. The accuracy of FIER medium-range water fraction pseudo-forecasts is slightly lower, with 70–80% of pixels exhibiting AEs < 30%. However, long-range water fraction forecasts exhibit notably lower accuracy, due to larger errors in the NWM long-range streamflow forecasts. In addition, the current FIER framework overlooks local snowmelt and direct rainfall, potentially introducing forecast errors. Finally, the quantile mapping method, which relies on pixel-by-pixel CDFs derived from historical FIER-synthesized and VIIRS-observed water fractions, may be less effective for pixels frequently obscured by clouds. Improvements could include bias correction of NWM forecasts, incorporating additional data sources to consider non-fluvial water sources, and refining the quantile mapping process with more observed water fractions.

In practical applications, FIER water fraction forecasts can potentially help farmers optimize fertilizing and planting practices, mitigating crop losses by proactively identifying flood-prone areas. Furthermore, by utilizing the downscaling methodology developed by [29,73], the 375 m FIER water fraction forecasts can be combined with high-resolution DEMs (e.g., 30 m SRTM DEM) to generate a corresponding high-resolution water depth forecast. This would aid in more accurate damage assessment and resource allocation [74].

Lastly, we highlight the potential for expanding the implementation of FIER to other flood-prone regions in the U.S., including ungauged basins. The global, continuously updated VIIRS-observed water fraction enables FIER to obtain spatiotemporal flood patterns in any flood-prone region. For the ungauged basins, the NWM retrospective streamflow data, archived on Amazon Web Services (https://registry.opendata.aws/nwm-archive/ (accessed on 17 September 2024)), can substitute for USGS in situ streamflow data in building the regression models. Applying bias correction techniques to the NWM retrospective streamflow data, such as the SABER method [60,61], could enhance the accuracy of streamflow data and subsequently FIER water fraction forecasting in these regions.

Supplementary Materials: The following supporting information can be downloaded at: Web application: https://fier-biascorrected-nwm-viirs.streamlit.app/ (accessed on 17 September 2024). Code: https://github.com/satellitehydrology/FIER_VIIRS_Process (accessed on 17 September 2024).

Author Contributions: Conceptualization, A.R., C.-H.C., H.L. and T.L.T.D.; methodology, A.R., C.-H.C., H.-H.W. and K.N.M.; software, A.R., C.-H.C. and H.-H.W.; validation, A.R. and C.-H.C.; formal analysis, A.R. and C.-H.C.; investigation, A.R. and C.-H.C.; resources, H.L., E.J.N., G.P.W., S.L., W.S.III, S.H. and A.L.G.; data curation, A.R., C.-H.C., H.-H.W., K.N.M. and S.L.; writing—original draft preparation, A.R. and C.-H.C.; writing—review and editing, H.L., T.L.T.D., E.J.N., G.P.W., K.N.M., S.L., W.S.III, S.H. and A.L.G.; visualization, A.R. and C.-H.C.; supervision, H.L.; project administration, H.L.; funding acquisition, H.L. and W.S.III. All authors have read and agreed to the published version of the manuscript.

Funding: This research was funded by NOAA JPSS Program, grant number NA20NES4320003, and the University of Houston GEAR Program.

Data Availability Statement: The daily VIIRS water fraction data are publicly available to download through AWS portal at https://noaa-jpss.s3.amazonaws.com/index.html#JPSS_Blended_Products/VFM_1day_GLB/ (accessed on 17 September 2024) and the Cooperative Institute for Meteorological Satellite Studies (CIMMS) portal at https://floods.ssec.wisc.edu/products/RIVER-FLDglobal-composite1 (accessed on 17 September 2024); developed by George Mason University (GMU). The USGS in situ streamflow data are available at https://maps.waterdata.usgs.gov/mapper/index.html (accessed on 17 September 2024). The NWM real-time forecasts are accessible through https://water.noaa.gov/about/nwm (accessed on), while the archived forecasts are stored in a Google Cloud Storage (GCS) at https://console.cloud.google.com/storage/browser/national-water-model;tab=objects?pli=1&prefix=&forceOnObjectsSortingFiltering=false (accessed on 17 September 2024). The USDA CDL data can also be freely downloaded from https://ipad.fas.usda.gov/countrysummary/Default.aspx?id=US (accessed on 17 September 2024).

Acknowledgments: We would like to acknowledge the NOAA JPSS Program for its support to this study. We are also grateful to the NOAA Office of Water Prediction and the Big Data program for making the NWM streamflow data publicly available.

Conflicts of Interest: The authors declare no conflicts of interest.

References

1. National Centers for Environmental Information. *U.S. Billion-Dollar Weather and Climate Disasters, 1980—Present*; National Centers for Environmental Information: Asheville, NC, USA, 2020. [CrossRef]
2. Tate, E.; Rahman, M.A.; Emrich, C.T.; Sampson, C.C. Flood Exposure and Social Vulnerability in the United States. *Nat. Hazards* **2021**, *106*, 435–457. [CrossRef]
3. Wing, O.E.J.; Lehman, W.; Bates, P.D.; Sampson, C.C.; Quinn, N.; Smith, A.M.; Neal, J.C.; Porter, J.R.; Kousky, C. Inequitable Patterns of US Flood Risk in the Anthropocene. *Nat. Clim. Chang.* **2022**, *12*, 156–162. [CrossRef]
4. Wing, O.E.J.; Bates, P.D.; Smith, A.M.; Sampson, C.C.; Johnson, K.A.; Fargione, J.; Morefield, P. Estimates of Present and Future Flood Risk in the Conterminous United States. *Environ. Res. Lett.* **2018**, *13*, 034023. [CrossRef]

5. Swain, D.L.; Wing, O.E.J.; Bates, P.D.; Done, J.M.; Johnson, K.A.; Cameron, D.R. Increased Flood Exposure Due to Climate Change and Population Growth in the United States. *Earths Future* **2020**, *8*, e2020EF001778. [CrossRef]
6. Speight, L.J.; Cranston, M.D.; White, C.J.; Kelly, L. Operational and Emerging Capabilities for Surface Water Flood Forecasting. *Wiley Interdiscip. Rev. Water* **2021**, *8*, e1517. [CrossRef]
7. Pappenberger, F.; Cloke, H.L.; Parker, D.J.; Wetterhall, F.; Richardson, D.S.; Thielen, J. The Monetary Benefit of Early Flood Warnings in Europe. *Environ. Sci. Policy* **2015**, *51*, 278–291. [CrossRef]
8. Teng, J.; Jakeman, A.J.; Vaze, J.; Croke, B.F.W.; Dutta, D.; Kim, S. Flood Inundation Modelling: A Review of Methods, Recent Advances and Uncertainty Analysis. *Environ. Model. Softw.* **2017**, *90*, 201–216. [CrossRef]
9. Bates, P.D. Flood Inundation Prediction. *Annu. Rev. Fluid. Mech.* **2021**, *54*, 287–315. [CrossRef]
10. Fraehr, N.; Wang, Q.J.; Wu, W.; Nathan, R. Development of a Fast and Accurate Hybrid Model for Floodplain Inundation Simulations. *Water Resour. Res.* **2023**, *59*, e2022WR033836. [CrossRef]
11. Fraehr, N.; Wang, Q.J.; Wu, W.; Nathan, R. Upskilling Low-Fidelity Hydrodynamic Models of Flood Inundation Through Spatial Analysis and Gaussian Process Learning. *Water Resour. Res.* **2022**, *58*, e2022WR032248. [CrossRef]
12. Krajewski, W.F.; Ceynar, D.; Demir, I.; Goska, R.; Kruger, A.; Langel, C.; Mantilllla, R.; Niemeier, J.; Quintero, F.; Seo, B.C.; et al. Real-Time Flood Forecasting and Information System for the State of Iowa. *Bull. Am. Meteorol. Soc.* **2017**, *98*, 539–554. [CrossRef]
13. Bates, P.D.; Pappenberger, F.; Romanowicz, R.J. Uncertainty in Flood Inundation Modelling. In *Applied Uncertainty Analysis for Flood Risk Management*; World Scientific: Singapore, 2014; pp. 232–269. [CrossRef]
14. Davidian, J. *Computation of Water-Surface Profiles in Open Channels*; Techniques of Water-Resources Investigations; USGS: Reston, VA, USA, 1984. [CrossRef]
15. Adams, T.E. Flood Forecasting in the United States NOAA/National Weather Service. In *Flood Forecasting: A Global Perspective*; Academic Press: Cambridge, MA, USA, 2016; pp. 249–310. [CrossRef]
16. Fraehr, N.; Wang, Q.J.; Wu, W.; Nathan, R. Supercharging Hydrodynamic Inundation Models for Instant Flood Insight. *Nat. Water* **2023**, *1*, 835–843. [CrossRef]
17. Ivanov, V.Y.; Xu, D.; Dwelle, M.C.; Sargsyan, K.; Wright, D.B.; Katopodes, N.; Kim, J.; Tran, V.N.; Warnock, A.; Fatichi, S.; et al. Breaking Down the Computational Barriers to Real-Time Urban Flood Forecasting. *Geophys. Res. Lett.* **2021**, *48*, e2021GL093585. [CrossRef]
18. Rennó, C.D.; Nobre, A.D.; Cuartas, L.A.; Soares, J.V.; Hodnett, M.G.; Tomasella, J.; Waterloo, M.J. HAND, a New Terrain Descriptor Using SRTM-DEM: Mapping Terra-Firme Rainforest Environments in Amazonia. *Remote Sens. Environ.* **2008**, *112*, 3469–3481. [CrossRef]
19. Nobre, A.D.; Cuartas, L.A.; Hodnett, M.; Rennó, C.D.; Rodrigues, G.; Silveira, A.; Waterloo, M.; Saleska, S. Height Above the Nearest Drainage—A Hydrologically Relevant New Terrain Model. *J. Hydrol.* **2011**, *404*, 13–29. [CrossRef]
20. Nobre, A.D.; Cuartas, L.A.; Momo, M.R.; Severo, D.L.; Pinheiro, A.; Nobre, C.A. HAND Contour: A New Proxy Predictor of Inundation Extent. *Hydrol. Process* **2016**, *30*, 320–333. [CrossRef]
21. Zheng, X.; Maidment, D.R.; Tarboton, D.G.; Liu, Y.Y.; Passalacqua, P. GeoFlood: Large-Scale Flood Inundation Mapping Based on High-Resolution Terrain Analysis. *Water Resour. Res.* **2018**, *54*, 10013–10033. [CrossRef]
22. Aristizabal, F.; Salas, F.; Petrochenkov, G.; Grout, T.; Avant, B.; Bates, B.; Spies, R.; Chadwick, N.; Wills, Z.; Judge, J. Extending Height Above Nearest Drainage to Model Multiple Fluvial Sources in Flood Inundation Mapping Applications for the U.S. National Water Model. *Water Resour. Res.* **2023**, *59*, e2022WR032039. [CrossRef]
23. Michael Johnson, J.; Munasinghe, D.; Eyelade, D.; Cohen, S. An Integrated Evaluation of the National Water Model (NWM)-Height above Nearest Drainage (HAND) Flood Mapping Methodology. *Nat. Hazards Earth Syst. Sci.* **2019**, *19*, 2405–2420. [CrossRef]
24. Smith, L.C. Satellite Remote Sensing of River Inundation Area, Stage, and Discharge: A Review. *Ltd. Hydrol. Process* **1997**, *11*, 1427–1439. [CrossRef]
25. Chang, C.H.; Lee, H.; Kim, D.; Hwang, E.; Hossain, F.; Chishtie, F.; Jayasinghe, S.; Basnayake, S. Hindcast and Forecast of Daily Inundation Extents Using Satellite SAR and Altimetry Data with Rotated Empirical Orthogonal Function Analysis: Case Study in Tonle Sap Lake Floodplain. *Remote Sens. Environ.* **2020**, *241*, 111732. [CrossRef]
26. Chang, C.H.; Lee, H.; Do, S.K.; Du, T.L.T.; Markert, K.; Hossain, F.; Ahmad, S.K.; Piman, T.; Meechaiya, C.; Bui, D.D.; et al. Operational Forecasting Inundation Extents Using REOF Analysis (FIER) over Lower Mekong and Its Potential Economic Impact on Agriculture. *Environ. Model. Softw.* **2023**, *162*, 105643. [CrossRef]
27. Red River Valley Farmers Look for Solutions to Three Generations of Cropland Flooding—Agweek | #1 Source for Agriculture News, Farming, Markets. Available online: https://www.agweek.com/business/red-river-valley-farmers-look-for-solutions-to-three-generations-of-cropland-flooding (accessed on 5 September 2024).
28. Heavy Rains Add to Farm Flooding in New Madrid, MO. Available online: https://www.kfvs12.com/2019/05/31/heavy-rains-add-farm-flooding-new-madrid-mo/ (accessed on 5 September 2024).
29. Li, S.; Sun, D.; Goldberg, M.D.; Kalluri, S.; Sjoberg, B.; Lindsey, D.; Hoffman, J.P.; DeWeese, M.; Connelly, B.; Mckee, P.; et al. A Downscaling Model for Derivation of 3-D Flood Products from VIIRS Imagery and SRTM/DEM. *ISPRS J. Photogramm. Remote Sens.* **2022**, *192*, 279–298. [CrossRef]
30. Li, S.; Sun, D.; Goldberg, M.D.; Sjoberg, B.; Santek, D.; Hoffman, J.P.; DeWeese, M.; Restrepo, P.; Lindsey, S.; Holloway, E. Automatic near Real-Time Flood Detection Using Suomi-NPP/VIIRS Data. *Remote Sens. Environ.* **2018**, *204*, 672–689. [CrossRef]

31. Kaur, G.; Singh, G.; Motavalli, P.P.; Nelson, K.A.; Orlowski, J.M.; Golden, B.R. Impacts and Management Strategies for Crop Production in Waterlogged or Flooded Soils: A Review. *Agron. J.* **2020**, *112*, 1475–1501. [CrossRef]
32. Atashi, V.; Rosati, M.; Lim, Y.H.; Taufique, M. Characteristics of Seasonality on 3D Velocity and Bathymetry Profiles in Red River of the North. In Proceedings of the World Environmental and Water Resources Congress 2022: Adaptive Planning and Design in an Age of Risk and Uncertainty—Selected Papers from the World Environmental and Water Resources Congress 2022, Atlanta, Georgia, 5–8 June 2022; pp. 252–263. [CrossRef]
33. What Makes the Red River of the North So Vulernable to Flooding? Available online: https://www.ndsu.edu/fargo_geology/whyflood.htm (accessed on 5 September 2024).
34. Roy, D.; Jia, X.; Steele, D.D.; Chu, X.; Lin, Z. Infiltration into Frozen Silty Clay Loam Soil with Different Soil Water Contents in the Red River of the North Basin in the USA. *Water* **2020**, *12*, 321. [CrossRef]
35. Rising Waters Along the Red River. Available online: https://earthobservatory.nasa.gov/images/50170/rising-waters-along-the-red-river (accessed on 5 September 2024).
36. Another Flood on the Red River. Available online: https://earthobservatory.nasa.gov/images/146616/another-flood-on-the-red-river (accessed on 5 September 2024).
37. Red River Flooding Is Worst in a Decade. Available online: https://earthobservatory.nasa.gov/images/149822/red-river-flooding-is-worst-in-a-decade (accessed on 5 September 2024).
38. Rajib, A.; Zheng, Q.; Golden, H.E.; Wu, Q.; Lane, C.R.; Christensen, J.R.; Morrison, R.R.; Annis, A.; Nardi, F. The Changing Face of Floodplains in the Mississippi River Basin Detected by a 60-Year Land Use Change Dataset. *Sci. Data* **2021**, *8*, 271. [CrossRef]
39. Gledhill, J.H.; Barnett, A.F.; Slattery, M.; Willett, K.L.; Easson, G.L.; Otts, S.S.; Gochfeld, D.J. Mass Mortality of the Eastern Oyster Crassostrea Virginica in the Western Mississippi Sound Following Unprecedented Mississippi River Flooding in 2019. *J. Shellfish. Res.* **2020**, *39*, 235–244. [CrossRef]
40. 2011 Mississippi River Flood Report Now Available > Mississippi Valley Division > News Releases. Available online: https://www.mvd.usace.army.mil/Media/News-Releases/Article/473851/2011-mississippi-river-flood-report-now-available/ (accessed on 5 September 2024).
41. Pal, S.; Lee, T.R.; Clark, N.E. The 2019 Mississippi and Missouri River Flooding and Its Impact on Atmospheric Boundary Layer Dynamics. *Geophys. Res. Lett.* **2020**, *47*, e2019GL086933. [CrossRef]
42. Pekel, J.F.; Cottam, A.; Gorelick, N.; Belward, A.S. High-Resolution Mapping of Global Surface Water and Its Long-Term Changes. *Nature* **2016**, *540*, 418–422. [CrossRef]
43. Section 4: Red River Valley | 4th Grade North Dakota Studies. Available online: https://www.ndstudies.gov/gr4/geology-geography-and-climate/part-2-geography/section-4-red-river-valley (accessed on 5 September 2024).
44. Wickham, J.; Stehman, S.V.; Sorenson, D.G.; Gass, L.; Dewitz, J.A. Thematic Accuracy Assessment of the NLCD 2019 Land Cover for the Conterminous United States. *GIsci. Remote Sens.* **2023**, *60*, 2181143. [CrossRef]
45. Goldberg, M.D.; Li, S.; Goodman, S.; Lindsey, D.; Sjoberg, B.; Sun, D. Contributions of Operational Satellites in Monitoring the Catastrophic Floodwaters Due to Hurricane Harvey. *Remote Sens.* **2018**, *10*, 1256. [CrossRef]
46. About National Water Model. Available online: https://water.noaa.gov/about/nwm (accessed on 5 September 2024).
47. United States Production. Available online: https://ipad.fas.usda.gov/countrysummary/Default.aspx?id=US (accessed on 5 September 2024).
48. Kaiser, H.F. The Varimax Criterion for Analytic Rotation in Factor Analysis. *Psychometrika* **1958**, *23*, 187–200. [CrossRef]
49. Hannachi, A. *A Primer for EOF Analysis of Climate Data*; Department of Meteorology, University of Reading: Reading, UK, 2004.
50. Imani, M.; You, R.J.; Kuo, C.Y. Caspian Sea Level Prediction Using Satellite Altimetry by Artificial Neural Networks. *Int. J. Environ. Sci. Technol.* **2014**, *11*, 1035–1042. [CrossRef]
51. Kim, T.; Yang, T.; Gao, S.; Zhang, L.; Ding, Z.; Wen, X.; Gourley, J.J.; Hong, Y. Can Artificial Intelligence and Data-Driven Machine Learning Models Match or Even Replace Process-Driven Hydrologic Models for Streamflow Simulation?: A Case Study of Four Watersheds with Different Hydro-Climatic Regions across the CONUS. *J. Hydrol.* **2021**, *598*, 126423. [CrossRef]
52. Maraun, D. Bias Correction, Quantile Mapping, and Downscaling: Revisiting the Inflation Issue. *J. Clim.* **2013**, *26*, 2137–2143. [CrossRef]
53. Enayati, M.; Bozorg-Haddad, O.; Bazrafshan, J.; Hejabi, S.; Chu, X. Bias Correction Capabilities of Quantile Mapping Methods for Rainfall and Temperature Variables. *J. Water Clim. Chang.* **2021**, *12*, 401–419. [CrossRef]
54. Markert, K.N.; Markert, A.M.; Mayer, T.; Nauman, C.; Haag, A.; Poortinga, A.; Bhandari, B.; Thwal, N.S.; Kunlamai, T.; Chishtie, F.; et al. Comparing Sentinel-1 Surface Water Mapping Algorithms and Radiometric Terrain Correction Processing in Southeast Asia Utilizing Google Earth Engine. *Remote Sens.* **2020**, *12*, 2469. [CrossRef]
55. Twele, A.; Cao, W.; Plank, S.; Martinis, S. Sentinel-1-Based Flood Mapping: A Fully Automated Processing Chain. *Int. J. Remote Sens.* **2016**, *37*, 2990–3004. [CrossRef]
56. Vollrath, A.; Mullissa, A.; Reiche, J. Angular-Based Radiometric Slope Correction for Sentinel-1 on Google Earth Engine. *Remote Sens.* **2020**, *12*, 1867. [CrossRef]
57. Yamazaki, D.; Ikeshima, D.; Tawatari, R.; Yamaguchi, T.; O'Loughlin, F.; Neal, J.C.; Sampson, C.C.; Kanae, S.; Bates, P.D. A High-Accuracy Map of Global Terrain Elevations. *Geophys. Res. Lett.* **2017**, *44*, 5844–5853. [CrossRef]
58. Lopes, A.; Touzi, R.; Nezry, E. Adaptive Speckle Filters and Scene Heterogeneity. *IEEE Trans. Geosci. Remote Sens.* **1990**, *28*, 992–1000. [CrossRef]

59. Lozano, J.S.; Bustamante, G.R.; Hales, R.C.; Nelson, E.J.; Williams, G.P.; Ames, D.P.; Jones, N.L.; Lozano, S.; Romero Bustamante, J.; Hales, G.; et al. A Streamflow Bias Correction and Performance Evaluation Web Application for GEOGloWS ECMWF Streamflow Services. *Hydrology* **2021**, *8*, 71. [CrossRef]
60. Hales, R.C.; Sowby, R.B.; Williams, G.P.; Nelson, E.J.; Ames, D.P.; Dundas, J.B.; Ogden, J. SABER: A Model-Agnostic Postprocessor for Bias Correcting Discharge from Large Hydrologic Models. *Hydrology* **2022**, *9*, 113. [CrossRef]
61. Hales, R.C.; Williams, G.P.; James Nelson, E.; Sowby, R.B.; Ames, D.P.; Lozano, J.L.S. Bias Correcting Discharge Simulations from the GEOGloWS Global Hydrologic Model. *J. Hydrol.* **2023**, *626*, 130279. [CrossRef]
62. Matsuyama, E.; Nishiki, M.; Takahashi, N.; Watanabe, H.; Matsuyama, E.; Nishiki, M.; Takahashi, N.; Watanabe, H. Using Cross Entropy as a Performance Metric for Quantifying Uncertainty in DNN Image Classifiers: An Application to Classification of Lung Cancer on CT Images. *J. Biomed. Sci. Eng.* **2024**, *17*, 1–12. [CrossRef]
63. Mittermaier, M.; Roberts, N.; Thompson, S.A. A Long-Term Assessment of Precipitation Forecast Skill Using the Fractions Skill Score. *Meteorol. Appl.* **2013**, *20*, 176–186. [CrossRef]
64. Bakurov, I.; Buzzelli, M.; Schettini, R.; Castelli, M.; Vanneschi, L. Structural Similarity Index (SSIM) Revisited: A Data-Driven Approach. *Expert Syst. Appl.* **2022**, *189*, 116087. [CrossRef]
65. Robertson, G.P.; Vitousek, P.M. Nitrogen in Agriculture: Balancing the Cost of an Essential Resource. *Annu. Rev. Environ. Resour.* **2009**, *34*, 97–125. [CrossRef]
66. Kopyra, M.; Gwóźdź, E.A. The Role of Nitric Oxide in Plant Growth Regulation and Responses to Abiotic Stresses. *Acta Physiol. Plant* **2004**, *26*, 459–473. [CrossRef]
67. Haddad, S.A.; Tabatabai, M.A.; Loynachan, T.E. Biochemical Processes Controlling Soil Nitrogen Mineralization under Waterlogged Conditions. *Soil. Sci. Soc. Am. J.* **2013**, *77*, 809–816. [CrossRef]
68. Ren, B.; Zhang, J.; Dong, S.; Liu, P.; Zhao, B. Root and Shoot Responses of Summer Maize to Waterlogging at Different Stages. *Agron. J.* **2016**, *108*, 1060–1069. [CrossRef]
69. Motavalli, P.P.; Goyne, K.W.; Udawatta, R.P. Environmental Impacts of Enhanced-Efficiency Nitrogen Fertilizers. *Crop Manag.* **2008**, *7*, 1–15. [CrossRef]
70. Noellsch, A.J.; Motavalli, P.P.; Nelson, K.A.; Kitchen, N.R. Corn Response to Conventional and Slow-Release Nitrogen Fertilizers across a Claypan Landscape. *Agron. J.* **2009**, *101*, 607–614. [CrossRef]
71. Liu, G.; Porterfield, D.M. Oxygen Enrichment with Magnesium Peroxide for Minimizing Hypoxic Stress of Flooded Corn. *J. Plant Nutr. Soil. Sci.* **2014**, *177*, 733–740. [CrossRef]
72. Bera, T.; Inglett, K.S.; Liu, G.D. Effects of Solid Oxygen Fertilizers and Biochars on Nitrous Oxide Production from Agricultural Soils in Florida. *Sci. Rep.* **2020**, *10*, 21754. [CrossRef]
73. Li, S.; Sun, D.; Goldberg, M.; Stefanidis, A. Derivation of 30-m-Resolution Water Maps from TERRA/MODIS and SRTM. *Remote Sens. Environ.* **2013**, *134*, 417–430. [CrossRef]
74. Peter, B.G.; Cohen, S.; Lucey, R.; Munasinghe, D.; Raney, A.; Brakenridge, G.R. Google Earth Engine Implementation of the Floodwater Depth Estimation Tool (FwDET-GEE) for Rapid and Large Scale Flood Analysis. *IEEE Geosci. Remote Sens. Lett.* **2022**, *19*, 1501005. [CrossRef]